

Light Magnetic Dark Matter in Direct Detection Searches

EUGENIO DEL NOBILE^{*}, CHRIS KOUVARIS[†], PAOLO PANCI[‡],
FRANCESCO SANNINO[§], JUSSI VIRKAJÄRVI^{**}

CP³-Origins and DIAS, University of Southern Denmark, Odense, Denmark

Abstract

We study a fermionic Dark Matter particle carrying magnetic dipole moment and analyze its impact on direct detection experiments. In particular we show that it can accommodate the DAMA, CoGeNT and CRESST experimental results. Assuming conservative bounds, this candidate is shown not to be ruled out by the CDMS, XENON and PICASSO experiments. We offer an analytic understanding of how the long-range interaction modifies the experimental allowed regions, in the cross section versus Dark Matter mass parameter space, with respect to the typically assumed contact interaction. Finally, in the context of a symmetric Dark Matter sector, we determine the associated thermal relic density, and further provide relevant constraints imposed by indirect searches and colliders.

Preprint: CP³-Origins-2012-007 & DIAS-2012-8

arXiv:1203.6652v2 [hep-ph] 13 Jul 2012

^{*}delnobile@cp3-origins.net

[†]kouvaris@cp3-origins.net

[‡]panci@cp3-origins.net

[§]sannino@cp3.dias.sdu.dk

^{**}virkajarvi@cp3-origins.net

Contents

| | | |
|----------|--|-----------|
| 1 | Introduction | 2 |
| 2 | The event rate | 4 |
| 2.1 | Kinematics | 4 |
| 2.2 | Model and differential cross section | 4 |
| 2.3 | Nuclear recoil rate | 6 |
| 3 | Theoretical predictions | 8 |
| 3.1 | Light Dark Matter | 11 |
| 3.2 | Heavy Dark Matter | 12 |
| 4 | Data sets and analysis technique | 13 |
| 5 | Fit to the direct detection experiments | 16 |
| 6 | Relic Abundance | 19 |
| 7 | Constraints | 21 |
| 7.1 | Epoch of reionization and CMB | 21 |
| 7.2 | Present epoch γ -rays | 22 |
| 7.3 | Collider and other Astrophysical constraints | 23 |
| 8 | Conclusions | 24 |
| A | Appendix | 24 |

1 Introduction

The presence of a relatively big dark component in the matter content of the Universe has been now established, and part of the scientific community is trying to unravel its still enigmatic properties. Despite the conspicuous number of experiments that probed the gravitational effects of this Dark Matter (DM) on the known matter, we still lack a more direct evidence of what it actually is and what are its properties.

Under the assumption that the DM is constituted by one or more unknown particles, several experiments have attempted recently to probe its microscopic nature and its interactions. Different search strategies are possible. For indirect detection experiments, traces of DM annihilations to known particles are looked for in cosmic rays or in the spectrum of solar neutrinos. Collider searches are also performed, in case the DM can be produced in sizable amounts to have an impact in the channels featuring missing energy. Direct detection experiments rely instead on direct scatterings of DM particles off nuclei of ordinary matter, inside shielded detectors placed underground in order to diminish the cosmic rays background.

DM direct detection experiments are providing exciting results. For example the DAMA/NaI collaboration [1] has claimed to have observed the expected annual modulation of the DM induced nuclear recoil rate [2,3], due to the rotation of the Earth around the Sun. The rotation, in fact, causes a different value of the flux of DM particles hitting the Earth depending on the different periods of the year. The upgraded DAMA/LIBRA detector has further confirmed [4] the earlier result adding much more statistics, and it has reached a significance of 8.9σ C.L. for the cumulative exposure [5].

Interestingly the DAMA annual modulation effect has been shown to be compatible with a DM interpretation which, for the case of coherent spin-independent scattering, leads to a range of DM masses spanning from a few GeV up to a few hundred GeV, and cross sections between 10^{-42} cm² to 10^{-39} cm² [1,4,5], with some noticeable differences due to the galactic halo modeling [6,7].

More recently, the CoGeNT experiment first reported an irreducible excess in the counting rate [8], which could also be in principle ascribed to a DM signal. In the last months, the same experiment reported an additional analysis which shows that the time-series of their rate is actually compatible with an annual modulation effect [9]. The evidence of such a modulation for CoGeNT is at the level of 2.8σ C.L.

Also the CRESST collaboration observed an excess [10]. In particular, 67 counts were found in the DM acceptance region, where the estimated background from leakage of e/γ events, neutrons, α particles and recoiling nuclei in α decays, is not sufficient to account for all the observed events. The analysis made by the collaboration rejects the background-only hypothesis at more than 4σ [10].

The interesting feature is that the DAMA and CoGeNT results appear to be compatible for relatively light DM particles, in the few GeV to tens of GeV mass range and coherent scattering cross section around 10^{-40} cm². CRESST points somehow to larger DM masses, but it is still compatible with the range determined by the other two experiments. The actual relevant range of masses and cross sections depends on assumptions of the galactic DM properties, namely the velocity distribution function and the local DM density [7]. Other relevant analyses can be found in Refs. [11–28].

The CDMS and XENON100 experiments have recently reported a small number of events which pass all the selection cuts. Specifically, they have 2 events for CDMS [29] and 6 events for XENON100, reduced to 3 events after post-selection analysis [30], which are

still too few to be interpreted as potential DM signal. They can therefore provide upper bounds on the DM scattering cross section. These constraints seem to set severe bounds on the DM parameter space, and therefore to rule out much of the allowed regions of the other experiments. Very recently the PICASSO experiment [31] seems to provide even more stringent constraints for the low mass DM interpretation of DAMA, CoGeNT and CRESST.

However, there are at least two caveats when interpreting the results from the experiments mentioned above. The first is that one has to pay attention to the fine details associated to the results quoted by each experiment, since a number of factors can affect the outcome. For example the actual response of the XENON and CDMS detectors can be uncertain and model dependent for a low energy signal [32–34]. Moreover, for crystal detectors like DAMA, an additional source of uncertainty is provided by the presence of an unknown fraction of nuclear recoils undergoing channeling. This effect is currently being investigated [35–37]. If confirmed, it would lead to a significant shift of the DAMA allowed regions in the DM parameter space. Another source of uncertainty is associated with the details of the nuclei form factors for each experiment.

The second caveat is associated to the interpretation of the actual data within a very simple-minded model of the DM interaction with nuclei. For example, for the spin-independent case it is often assumed that DM couples via a contact interaction with equal strength to the proton and neutron. Upon relaxing some of these assumptions, less stringent constraints can be drawn.

In this work we perform a thorough investigation of the effects of a magnetic dipole moment of the DM on the direct detection experiments. We refer to [23, 38–50] for a limited sample of the earlier literature.

A fermionic DM particle with a magnetic dipole moment can arise for example in models of composite DM [51–53], or more generally in models featuring a new strong interaction (see e.g. [54]). The application to cosmic rays as well as a complete discussion also of the light asymmetric DM paradigm, and last, but not the least, the first link to the study of grand unifications using DM appeared in [55]. Recently it was shown, for the first time, via first principle lattice simulations [56] that one has, indeed, for minimal models of Technicolor the correct pattern of chiral symmetry breaking leading to natural candidates of light composite DM. Despite the possibility to link the DM issue to other unresolved fundamental questions like e.g. the (dynamical) breaking of the Electroweak symmetry or to the grand unification problem, we investigate this DM candidate in a model independent way addressing only its DM phenomenology. The main feature of the present DM candidate is that it couples mainly to the photon and therefore interacts mostly with protons, and secondly and more importantly it has long-range type interactions modifying substantially the recoil spectrum with respect to a contact interaction. In fact, as pointed out in [57], low-energy threshold detectors like CoGeNT and DAMA are especially sensitive to this kind of interaction, and therefore the hope exists to get a better agreement among the various direct detection experiments.

Here we will show how the DM magnetic moment interaction affects the interpretation of the different direct detection experiments. In Sec. 2 we present the DM interaction Lagrangian and provide some considerations concerning the scattering of DM off nuclei. This will allow us to determine the nuclear recoil rate for a given experiment. In Sec. 3 we show how the experimental favored regions and constraints are modified with respect to the naïve contact interaction case. In Sec. 4 we describe the experimental data set we use and

our statistical analysis performed to determine the favored regions and constraints for the DM candidate envisioned here. We summarize these results in Sec. 5. We determine the associated thermal relic density Sec. 6, and in Sec. 7 we report the constraints imposed by indirect searches, colliders and by the observations of compact stars. Finally, we conclude in Sec. 8.

2 The event rate

2.1 Kinematics

When a DM particle scatters off a nucleus, depending on the DM properties, one can envision at least two distinct kinematics, the elastic and the inelastic. The elastic scattering is represented by

$$\chi + \mathcal{N}(A, Z)_{\text{at rest}} \rightarrow \chi + \mathcal{N}(A, Z)_{\text{recoil}} , \quad (1)$$

while the inelastic is

$$\chi + \mathcal{N}(A, Z)_{\text{at rest}} \rightarrow \chi' + \mathcal{N}(A, Z)_{\text{recoil}} . \quad (2)$$

In (1) and (2), χ and χ' are two DM particle states, and A, Z are respectively the mass and atomic numbers of the nucleus \mathcal{N} . In the detector rest frame, a DM particle with velocity v and mass m_χ can scatter off a nucleus of mass m_N , causing it to recoil. The minimal velocity providing a recoil energy E_R is:

$$v_{\min}(E_R) \simeq \sqrt{\frac{m_N E_R}{2\mu_{\chi N}^2}} \left(1 + \frac{\mu_{\chi N} \delta}{m_N E_R} \right) , \quad (3)$$

where $\mu_{\chi N}$ is the DM-nucleus reduced mass and $\delta = m'_\chi - m_\chi$ is the mass splitting between χ and χ' , and the equation above holds for $\delta \ll m'_\chi, m_\chi$. Elastic scattering occurs for $\delta = 0$, while $\delta \neq 0$ implies inelastic scattering. In this paper we will only consider the case of elastic scattering.

2.2 Model and differential cross section

We concentrate on the possibility of having a massless mediator of the DM-nuclei interaction able to yield long-range interactions absent in contact interactions usually assumed. The obvious candidate mediator in the SM is the photon while other exotic possibilities can be also envisioned such as a dark photon, see e.g. [57, 58].

Assuming that the dark matter is either a neutral boson or fermion one can then use the language of the effective theories to select the relevant operators. Stability of the specific candidate can be easily ensured by charging it under an unbroken global symmetry. The most popular choices are either a new $U(1)$ or a \mathbb{Z}_2 depending on the reality of the specific candidate DM field.

In [59] one can find a general classification, up to dimension six, of all the possible interactions between a scalar DM and the SM fields. To this order one discovers that there is only one gauge-invariant operator coupling the DM complex boson to a photon, namely

$$i(\varphi^\dagger \overleftrightarrow{\partial}_\mu \varphi) \partial_\nu F^{\mu\nu} ; \quad (4)$$

DM-nucleus scattering mediated by this operator has been studied for instance in Ref. [18, 60, 61], where it is shown that it actually leads to a contact interaction and will henceforth not be used here.

On the other hand, considering a fermionic DM χ one can show that the only gauge-invariant couplings to the photon, up to dimension five, are the magnetic and electric moment-mediated interactions:

$$\mathcal{L}_M^{\text{int}} = -\frac{1}{2}\lambda_\chi \bar{\chi}\sigma_{\mu\nu}\chi F^{\mu\nu} , \quad \mathcal{L}_E^{\text{int}} = -\frac{1}{2}i d_\chi \bar{\chi}\sigma_{\mu\nu}\gamma^5\chi F^{\mu\nu} . \quad (5)$$

For a Majorana fermion both $\mathcal{L}_M^{\text{int}}$ and $\mathcal{L}_E^{\text{int}}$ vanish identically, therefore χ has to be a Dirac fermion. λ_χ and d_χ are the magnetic and electric dipole moment, respectively, and are usually expressed in units of $e \times \text{cm}$. The scales $\Lambda_M \equiv e/\lambda_\chi$ and $\Lambda_E \equiv e/d_\chi$ can be interpreted as the energy scales of the underlying interaction responsible for the associated operators to arise. For instance, in models in which the interactions (5) are explained by the DM being a bound state of charged particles, the Λ 's could represent the compositeness scale.

The differential cross sections for elastic scattering are [41]

$$\frac{d\sigma_M(v, E_R)}{dE_R} = \frac{d\sigma_M^{\text{SI}}(v, E_R)}{dE_R} + \frac{d\sigma_M^{\text{SD}}(v, E_R)}{dE_R} = \frac{\alpha\lambda_\chi^2}{E_R} \left\{ Z^2 \left[1 - \frac{E_R}{v^2} \left(\frac{2m_N + m_\chi}{2m_N m_\chi} \right) \right] F_{\text{SI}}^2(E_R) + \left(\frac{\bar{\lambda}_{\text{nuc}}}{\lambda_p} \right)^2 \frac{E_R}{v^2} \frac{m_N}{3m_p^2} F_{\text{SD}}^2(E_R) \right\} , \quad (6)$$

$$\frac{d\sigma_E(v, E_R)}{dE_R} = \frac{\alpha Z^2}{E_R v^2} d_\chi^2 F_{\text{SI}}^2(E_R) , \quad (7)$$

where v is the speed of the DM particle in the Earth frame, $\alpha = e^2/4\pi \simeq 1/137$ is the fine structure constant, $\lambda_p = e/2m_p$ is the nuclear magneton and F_{SI} (F_{SD}) denotes the spin-independent (spin-dependent) nuclear form factor which takes into account the finite dimension of the nucleus. Here

$$\bar{\lambda}_{\text{nuc}} = \left(\sum_{\text{isotopes}} f_i \mu_i^2 \frac{S_i + 1}{S_i} \right)^{1/2} , \quad (8)$$

is the weighted dipole moment of the target [42], where f_i , μ_i and S_i are respectively the abundance, nuclear magnetic moment and spin of the i -th isotope; the values for these quantities are taken from [62, 63] and agree exactly with the values provided in Fig. 1 of [42].

The differential cross section in (6) features both a spin-independent (SI) and a spin-dependent (SD) part. The SI part, neglecting for a moment the form factor, contains two terms: an energy dependent term with a E_R^{-1} drop-off of the cross section, and an energy independent one. In contrast the common contact interactions only feature the constant term, typically with the $1/v^2$ dependence on the DM velocity; the SD part is of this kind. Notice that, for low enough energies (that might be also below threshold for some experiments, in principle), the interaction is always SI due to the E_R^{-1} divergence. As the recoil energy rises, the interaction becomes mostly SD for target nuclei with large magnetic moment, namely ^{19}F , ^{23}Na and ^{127}I , ($\bar{\lambda}_{\text{nuc}}/\lambda_p = 4.55, 2.86, 3.33$ respectively); the SD term is instead negligible for all the other nuclei.

The differential cross section in (7), instead, has only an energy dependent term. We observe that the cross section in the electric case is enhanced with respect to the magnetic one by a factor $1/v^2 \sim 10^6$ translating in a value for d_χ circa 10^3 times lower than the one for λ_χ , when one tries to fit the experiments. This is confirmed for instance by Ref. [41], where the authors find that, in order to fit the CoGeNT data alone, a Λ_M of the order of the TeV is needed for a magnetic moment interaction, while for electric moment interaction Λ_E is around the PeV. Given that such a high scale is hardly reconcilable with other attempts to study DM and in general new physics, we will treat from now on only the magnetic dipole moment interaction $\mathcal{L}_M^{\text{int}}$.

As for F_{SI} and F_{SD} , we use the nuclear form factors provided in Ref. [64]. For the SI interaction we have checked that F_{SI} matches with the standard Helm form factor [65]. We recall that all the parameters used in the parameterization of the nuclear form factors may be affected by sizable uncertainties.

2.3 Nuclear recoil rate

The differential recoil rate of a detector can be defined as:

$$\frac{dR}{dE_R} = N_T \int \frac{d\sigma_M(v, E_R)}{dE_R} v dn_\chi, \quad (9)$$

where $N_T = N_A/A$ is the total number of targets in the detector (N_A is the Avogadro's number) and dn_χ is the local number density of DM particles with velocities in the elemental volume d^3v around \vec{v} . This last factor can be expressed as a function of the DM velocity distribution $f_E(\vec{v})$ in the Earth frame, which is related to the DM velocity distribution in the galactic frame $f_G(\vec{w})$ by the galilean velocity transformation $f_E(\vec{v}) = f_G(\vec{v} + \vec{v}_E(t))$; here $\vec{v}_E(t)$ is the time-dependent Earth (or detector) velocity with respect to the galactic frame. The prominent time-dependence (on the time-scale of an experiment) comes from the annual rotation of the Earth around the Sun, which is the origin of the annual modulation effect of the direct detection rate [2, 3]. More specifically:

$$\vec{v}_E(t) = \vec{v}_G + \vec{v}_S + \vec{v}_\oplus(t). \quad (10)$$

The galactic rotational velocity of our local system \vec{v}_G and the Sun's proper motion \vec{v}_S are basically aligned and their absolute values are $v_G \equiv v_0 = 220 \pm 50$ km/s and $v_S = 12$ km/s, while the Earth rotational velocity $\vec{v}_\oplus(t)$ has a size $v_\oplus = 30$ km/s, period of 1 year and phase such that it is aligned to \vec{v}_G around June 2nd and it is inclined of an angle $\gamma \simeq 60^\circ$ with respect to the galactic plane. More details can be found, for instance, in Ref. [66]. Summarizing:

$$dn_\chi = n_\chi f_E(\vec{v}) d^3v, \quad (11)$$

where $n_\chi = \xi_\chi \rho_0 / m_\chi$ is the local DM number density in the Galaxy and is determined by the local Dark Matter density ρ_0 and, in general, by a scaling factor ξ_χ which accounts for the possibility that the specific DM candidate under consideration does not represent the whole amount of DM. Here we assume $\xi_\chi = 1$. In Eq. (11) the velocity distribution function needs to be properly normalized: this can be achieved by requiring that in the galactic frame

$$\int_{v \leq v_{\text{esc}}} d^3v f_G(\vec{v}) = 1, \quad (12)$$

where v_{esc} denotes the escape velocity of DM particles in the Milky Way. For definiteness, we will adopt here $v_{\text{esc}} = 650$ km/s.

When considering the differential cross section given in equation (6), the rate of nuclear recoils reduces to

$$\frac{dR}{dE_R}(t) = N_A \frac{\xi_X \rho_0}{A m_\chi} \frac{\alpha \lambda_X^2}{E_R} \left(Z^2 \mathcal{G}_{\text{SI}}(v_{\text{min}}, t) F_{\text{SI}}^2(E_R) + (\bar{\lambda}_{\text{nuc}}/\lambda_p)^2 \mathcal{G}_{\text{SD}}(v_{\text{min}}, t) F_{\text{SD}}^2(E_R) \right), \quad (13)$$

where

$$\mathcal{G}_{\text{SI}}(v_{\text{min}}(E_R), t) = \mathcal{I}(v_{\text{min}}(E_R), t) \left[\frac{\mathcal{I}_1(v_{\text{min}}(E_R), t)}{\mathcal{I}(v_{\text{min}}(E_R), t)} - E_R \left(\frac{2m_N + m_\chi}{2m_N m_\chi} \right) \right], \quad (14)$$

$$\mathcal{G}_{\text{SD}}(v_{\text{min}}(E_R), t) = \mathcal{I}(v_{\text{min}}(E_R), t) \frac{m_N E_R}{3m_p^2}, \quad (15)$$

and

$$\mathcal{I}(v_{\text{min}}, t) = \int_{v \geq v_{\text{min}}(E_R)} d^3v \frac{f_{\text{E}}(\vec{v})}{v}, \quad \mathcal{I}_1(v_{\text{min}}, t) = \int_{v \geq v_{\text{min}}(E_R)} d^3v v f_{\text{E}}(\vec{v}), \quad (16)$$

with $v_{\text{min}}(E_R)$ given by Eq. (3). The detection rate is function of time through the velocity integrals $\mathcal{I}(v_{\text{min}}, t)$ and $\mathcal{I}_1(v_{\text{min}}, t)$ as a consequence of the annual motion of the Earth around the Sun. Their actual form depends on the velocity distribution function of the DM particles in the halo. In this paper we will consider an isothermal sphere density profile for the DM, whose velocity distribution function in the galactic frame is a truncated Maxwell-Boltzmann:

$$f_{\text{G}}(\vec{v}) = \frac{\exp(-v^2/v_0^2)}{(v_0 \sqrt{\pi})^3 \text{erf}(v_{\text{esc}}/v_0) - 2v_0^3 \pi (v_{\text{esc}}/v_0) \exp(-v_{\text{esc}}^2/v_0^2)}. \quad (17)$$

Under this assumption, and defining the normalized velocities $\eta_\odot \equiv (v_{\text{G}} + v_{\text{S}})/v_0 \equiv v_\odot/v_0$, $\eta_{\text{E}}(t) \equiv v_{\text{E}}(t)/v_0$, $\eta_{\text{min}}(E_R) \equiv v_{\text{min}}(E_R)/v_0$ and $\eta_{\text{esc}} \equiv v_{\text{esc}}/v_0$, the velocity integrals can be written analytically as [41]

$$\mathcal{I}(\eta_{\text{min}}, t) = \frac{1}{2 v_0 \eta_{\text{E}}(t)} [\text{erf}(\eta_+) - \text{erf}(\eta_-)] - \frac{1}{\sqrt{\pi} v_0 \eta_{\text{E}}(t)} (\eta_+ - \eta_-) e^{-\eta_{\text{esc}}^2} \quad (18)$$

and

$$\begin{aligned} \mathcal{I}_1(\eta_{\text{min}}, t) = v_0 \left[\left(\frac{\eta_-}{2\sqrt{\pi} \eta_{\text{E}}(t)} + \frac{1}{\sqrt{\pi}} \right) e^{-\eta_-^2} - \left(\frac{\eta_+}{2\sqrt{\pi} \eta_{\text{E}}(t)} - \frac{1}{\sqrt{\pi}} \right) e^{-\eta_+^2} \right] \\ + \frac{v_0}{4 \eta_{\text{E}}(t)} (1 + 2\eta_{\text{E}}^2(t)) [\text{erf}(\eta_+) - \text{erf}(\eta_-)] \\ - \frac{v_0}{\sqrt{\pi}} \left[2 + \frac{1}{3\eta_{\text{E}}(t)} ((\eta_{\text{min}} + \eta_{\text{esc}} - \eta_-)^3 - (\eta_{\text{min}} + \eta_{\text{esc}} - \eta_+)^3) \right] e^{-\eta_{\text{esc}}^2}, \end{aligned} \quad (19)$$

where $\eta_\pm(E_R) = \min(\eta_{\text{min}}(E_R) \pm \eta_{\text{E}}, \eta_{\text{esc}})$.

Since in Eq. (10) the rotational velocity of the Earth around the Sun v_\oplus , is relatively small compared to the main contribution represented by $v_{\text{G}} + v_{\text{S}}$, we can approximate $\vec{v}_{\text{E}}(t)$ with its component directed toward the galactic center. We can then write [66]

$$\eta_{\text{E}}(t) \simeq \eta_\odot + \Delta\eta \cos[2\pi(t - \phi)/\tau], \quad (20)$$

where $\Delta\eta = v_{\oplus} \cos \gamma / v_0$, with $\Delta\eta \ll \eta_{\odot}$, and where $\phi = 152.5$ days (June 2nd) is the phase and $\tau = 365$ days is the period of the Earth motion around the Sun. By means of Eq. (20) we can then expand the recoil rate, assuming that the velocity distribution is not strongly anisotropic:

$$\frac{dR}{dE_R}(t) \simeq \left. \frac{dR}{dE_R} \right|_{\eta_E = \eta_{\odot}} + \frac{\partial}{\partial \eta_E} \left. \frac{dR}{dE_R} \right|_{\eta_E = \eta_{\odot}} \Delta\eta \cos [2\pi(t - \phi)/\tau] . \quad (21)$$

To properly reproduce the recoil rate measured by the experiments, we should take into account the effect of partial recollection of the released energy (quenching), and the energy resolution of the detector:

$$\frac{dR}{dE_{\text{det}}}(E_{\text{det}}) = \int dE' \mathcal{K}(E_{\text{det}}, E') \sum_i \frac{dR_i}{dE_R} \left(E_R = \frac{E'}{q_i} \right) . \quad (22)$$

Here the index i denotes different nuclear species in the detector, E_{det} is the detected energy and q_i are the quenching factors for each of the nuclear species. The function $\mathcal{K}(E_{\text{det}}, E')$ reproduces the effect of the energy resolution of the detector; as is generally done, we assume for it a Gaussian behavior.

Finally, the recoil rate of Eq. (22) must be averaged over the energy bins of the detector. For each energy bin k of width ΔE_k we therefore define the unmodulated components of the rate S_{0k} and the modulation amplitudes S_{mk} as:

$$S_{0k} = \frac{1}{\Delta E_k} \int_{\Delta E_k} dE_{\text{det}} \left. \frac{dR}{dE_{\text{det}}} \right|_{\eta_E = \eta_{\odot}} , \quad (23)$$

$$S_{mk} = \frac{1}{\Delta E_k} \int_{\Delta E_k} dE_{\text{det}} \left. \frac{\partial}{\partial \eta_E} \frac{dR}{dE_{\text{det}}} \right|_{\eta_E = \eta_{\odot}} \Delta\eta . \quad (24)$$

S_{0k} and S_{mk} are the relevant quantities that we use for the analysis of the experiments which address the annual modulation effect, namely DAMA and CoGeNT. For the other experiments, only the S_{0k} are relevant.

3 Theoretical predictions

We attempt here an analytical study of the effect of the magnetic moment interaction on the observed differential rate. More precisely we provide a simple comparison between the results arising from the interaction studied here and the *standard* picture, i.e. the spin-independent coherent contact interaction, shown in Fig. 1. To this aim, Eq. (13) can be rewritten as

$$\frac{dR}{dE_R}(t) = N_A \frac{\xi_{\chi} \rho_0}{A m_{\chi}} \frac{m_N}{2\mu_{\chi n}^2} A^2 \alpha \lambda_{\chi}^2 \Theta(E_R) \mathcal{I}(\eta_{\min}(E_R), t) F_{\text{SI}}^2(E_R) , \quad (25)$$

where $\mu_{\chi n}$ is the DM-nucleon reduced mass, $\alpha \lambda_{\chi}^2$ plays the role of the spin-independent DM-proton cross section σ_p and we defined

$$\Theta(E_R) = \Theta_{\text{SI}}(E_R) \left(1 + \frac{\Theta_{\text{SD}}(E_R) F_{\text{SD}}^2(E_R)}{\Theta_{\text{SI}}(E_R) F_{\text{SI}}^2(E_R)} \right) = \Theta_{\text{SI}}(E_R) (1 + r(E_R)) , \quad (26)$$

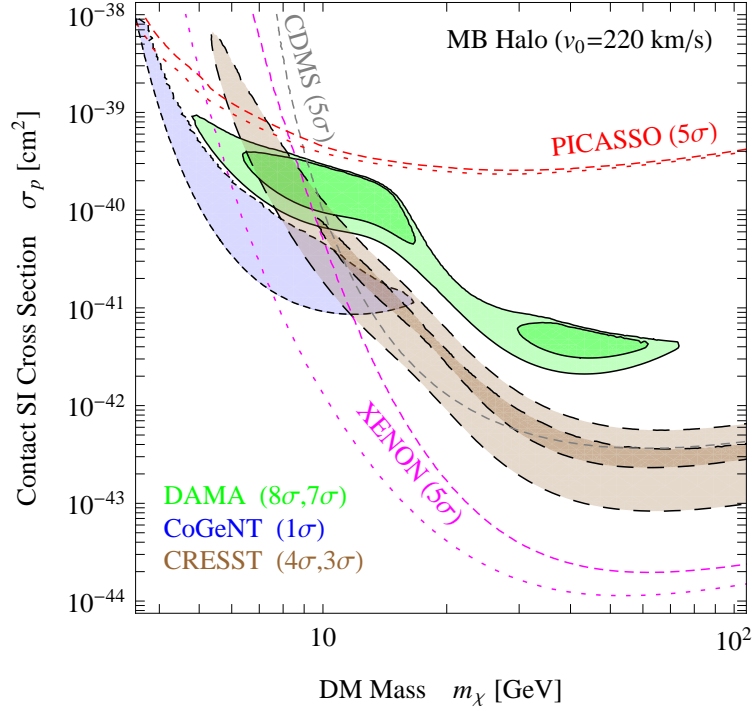


Figure 1: DM-proton spin-independent interaction cross section σ_p as a function of the Dark Matter mass m_χ , in the “standard” case of coherent contact interaction. The galactic halo has been assumed in the form of an isothermal sphere with velocity dispersion $v_0 = 220$ km/s and local density $\rho_0 = 0.3$ GeV/cm³. In this figure we show the allowed regions compatible with the annual modulation effects in DAMA and CoGeNT, as well as the region compatible with the CRESST excess, when interpreted as a DM signal. Specifically, the solid green contours denote the regions compatible with the DAMA annual modulation effect [4, 5], in absence of channeling [35]. The short-dashed blue contour refers to the region derived from the CoGeNT annual modulation effect [9], when the bound from the unmodulated CoGeNT data is included. The dashed brown contours denote the regions compatible with the CRESST excess [10]. For all the data sets, the contours refer to regions where the absence of excess can be excluded with a C.L. of 7σ (outer region), 8σ (inner region) for DAMA, 1σ for CoGeNT and 3σ (outer region), 4σ (inner region) for CRESST. For XENON, the constraints refer to a threshold of 4 photoelectrons (published value [30], lower line) and 8 photoelectrons (our conservative estimate, upper line), as discussed in Sec. 4. The two lines for PICASSO enclose the uncertainty in the energy resolution [31].

where

$$\Theta_{\text{SI}}(E_R) = \left(\frac{Z}{A}\right)^2 \left(\frac{2\mu_{\chi n}^2}{m_N E_R}\right) \left(\frac{\mathcal{G}_{\text{SI}}(\eta_{\min}(E_R), t)}{\mathcal{I}(\eta_{\min}(E_R), t)}\right), \quad (27)$$

$$\Theta_{\text{SD}}(E_R) = \left(\frac{1}{A}\right)^2 \left(\frac{\bar{\lambda}_{\text{nuc}}}{\lambda_p}\right)^2 \left(\frac{2\mu_{\chi n}^2}{m_N E_R}\right) \left(\frac{\mathcal{G}_{\text{SD}}(\eta_{\min}(E_R), t)}{\mathcal{I}(\eta_{\min}(E_R), t)}\right) = \frac{2}{3} \left(\frac{1}{A}\right)^2 \left(\frac{\bar{\lambda}_{\text{nuc}}}{\lambda_p}\right)^2 \left(\frac{\mu_{\chi n}}{m_p}\right)^2. \quad (28)$$

The function Θ measures the deviation of the allowed regions and constraints with respect to the standard spin-independent picture, and the ratio r parametrizes the relevance of the

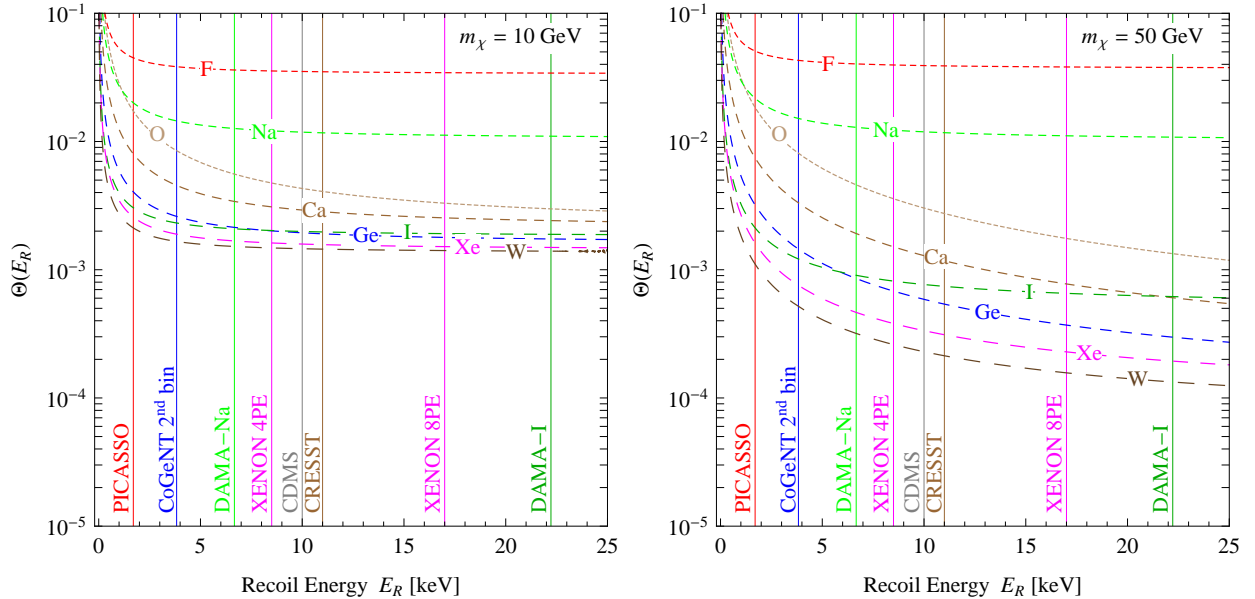


Figure 2: The function $\Theta(E_R)$ (dashed lines), parametrizing the deviation of the allowed regions and constraints with respect to the standard case of contact interaction without isospin violation presented in Fig. 1. Each line is for one of the target elements used in the experiments taken into account in the text. The vertical lines indicate the low energy thresholds for the various experiments (apart from CoGeNT, for which we show the threshold of the second energy bin, where much of the signal is recorded). For DAMA two thresholds are shown, corresponding to the corrections due to the quenching factors for sodium ($q_{\text{Na}} = 0.3$, in the assumption of scattering mainly off Na) and iodine ($q_{\text{I}} = 0.09$, for the assumption of scattering mainly off I). For XENON the 4 photoelectrons (4PE, published value [30]) and 8 photoelectrons (8PE, our conservative estimate) thresholds are shown, as discussed in Sec. 4. We have shown also the lowest threshold for the PICASSO experiment, although we refer to the main text for a more precise interpretation of its temperature dependent thresholds. The picture is reported for two values of the DM mass, $m_\chi = 10$ GeV (left panel) and $m_\chi = 50$ GeV (right panel).

SD interaction respect to the SI one: if $r > 1$ the interaction is largely SD, while it is mostly SI for $r < 1$ (see Appendix A for a more detailed analysis).

Since $\mathcal{G}_{\text{SI}}/\mathcal{I}$ depends itself on m_χ , we expect an asymmetric shift of the favored regions and constraint lines in the (m_χ, σ_p) plane due exclusively to the modified dynamics of the interaction considered here. There are only two free parameters in this model: m_χ , and σ_p (or alternatively λ_χ). This is not true for instance in models with contact interaction in which the DM interacts differently with protons and with neutrons (the so-called “isospin violating” scenario, see e.g. [17, 18, 22, 58, 67–74]). Indeed in such models the role of Θ is played by the expression $([Z + f_n/f_p(A - Z)]/A)^2$, and therefore there are three free parameters that must be fitted: σ_p , m_χ , and the ratio of the DM-neutron and DM-proton couplings f_n/f_p .

In Fig. 2 we show the behavior of Θ as a function of E_R both for small (left panel) and large (right panel) DM masses, considering several targets, $v_0 = 220$ km/s and $v_E = v_\odot$ (being $v_\oplus \cos \gamma \ll v_\odot$). In order to simplify the reading of the figures, we take the limit $v_{\text{esc}} \rightarrow \infty$; one can figure out the effect of a finite escape velocity as a target-dependent cut-off at high recoil energies, that sets in when the minimum velocity required to have a

recoil above threshold exceeds $v_{\text{esc}} + v_{\text{E}}$, the maximum escape velocity in the Earth frame. There, the function Θ loses its meaning since the expected rate is zero both in the standard picture and in the case considered here.

A first striking feature of Θ is its overall magnitude: depending on the DM mass and on the experiment, we have in fact a suppression of the expected rate of roughly 1 to 4 orders of magnitude. For nuclei in which the interaction is mostly SD ($r > 1$), Θ provides a suppression of 1 to 3 orders of magnitude for the well known reason that the rate does not carry any A^2 factor, contrarily to the usual SI case. Due to this fact, the SD part of the cross section is usually considered negligible respect to the SI one, but this turns out to be false in our case, for nuclei with large magnetic moment, since also the SI part is strongly suppressed. This suppression is due to the interplay of the last two factors in Eq. (27), while the first term plays only a marginal role given that $A \sim 2Z$ roughly for all the target nuclei. The second term, $2\mu_{\chi n}^2/m_N E_R$, enhances Θ by 2 to 4 orders of magnitude due to the presence of E_R , whose typical scale is few (tens of) keV and therefore very small compared to all the other mass scales involved. The last term $\mathcal{G}_{\text{SI}}/\mathcal{I}$, containing the velocity integrals, gives instead a suppression of roughly 6 orders of magnitude. Given the measured rate, this overall suppression provided by the Θ function will reflect in the fit pointing to higher interaction cross sections, with respect to the standard case of Fig. 1. This fact will play a role in fitting the relic abundance (Sec. 6).

The steep rise at low energies is always due to the long-range type of the SI part of the interaction, being the SD one of a contact type; in the particular case of magnetic dipole moment interaction considered here, the differential cross section diverges as $1/E_R$. At energies higher than the steep rise, for nuclei with large magnetic moment ($r > 1$), the interaction rapidly becomes of a contact type and therefore the function Θ exhibits a plateau whose value is $\sim (\bar{\lambda}_{\text{nuc}}/A\lambda_p)^2$. Instead, for the other nuclei for which $r < 1$, two regimes are possible, depending on the ratio $v_{\text{min}}/v_{\text{E}}$. These reflect the two trends assumed by the function¹ $\zeta(v_{\text{min}}) \equiv \mathcal{I}_1(v_{\text{min}})/\mathcal{I}(v_{\text{min}})$, namely a plateau $\zeta \sim 1.8 v_0^2$ for $v_{\text{min}} \ll v_{\text{E}}$ and a rise $\zeta \sim v_{\text{min}}^2$ for $v_{\text{min}} \gg v_{\text{E}}$, with an intermediate value of $\zeta(v_{\text{E}}) \sim 2.8 v_0^2$.

Light DM particles require a higher minimum velocity to recoil compared to heavier ones. For the range of DM masses we are interested in, and for the range of recoil energies relevant for the direct DM search experiments, the value of $v_{\text{min}}/v_{\text{E}}$ is controlled by the ratio m_N/m_χ . We will see that, depending on this ratio, the function Θ_{SI} can assume a constant behavior or scale as E_R^{-1} , while the function Θ_{SD} is always constant.

3.1 Light Dark Matter

For DM particles much lighter than the target nuclei, we have that $v_{\text{min}} > v_{\text{E}}$ already at low energies for all the targets considered, and therefore

$$\frac{\mathcal{G}_{\text{SI}}(\eta_{\text{min}}(E_R), t)}{\mathcal{I}(\eta_{\text{min}}(E_R), t)} \simeq \left[v_{\text{min}}^2(E_R) - E_R \left(\frac{2m_N + m_\chi}{2m_N m_\chi} \right) \right] = \frac{m_N E_R}{2m_\chi^2}; \quad (29)$$

accordingly, Θ simplifies to $(\mu_{\chi n}/(A m_p))^2 \left[Z^2 (m_p/m_\chi)^2 + 2/3 (\bar{\lambda}_{\text{nuc}}/\lambda_p)^2 \right]$, displaying the plateau shown in the left panel of Fig. 2. As expected, the plateau sets in earlier for heavy targets if the SI interaction dominates ($Z^2 (m_p/m_\chi)^2 \gg 2/3 (\bar{\lambda}_{\text{nuc}}/\lambda_p)^2$), while its starting

¹Here we ignore the time dependence, which gives only a negligible contribution.

point is independent on the target mass for SD interactions. We notice that, for high enough recoil energies, Θ always gets to this constant behavior; it is interesting though that it exists a regime in which this happens at the low energies relevant for DM direct detection experiments. An indicative $m_\chi \sim 10$ GeV falls into this case, and as we will show in Sec. 5 can fit the regions of the parameter space allowed by CoGeNT, DAMA-Na, CRESST-O and CRESST-Ca².

For an experiment with a lower threshold above the steep rise, the differential rate does not feature any dependence on E_R and it is therefore similar to the rate of spin-independent contact interactions, apart from a different functional dependence on m_χ . Notice that due to this different dependence on the mass of the DM, the rate is more suppressed for heavier DM particles, and therefore we expect the favored regions in the (m_χ, σ_p) plane as well as the exclusion lines to raise and slightly tilt at higher m_χ (compared to the spin-independent contact interaction).

Considering now that most of the signal in a given detector comes generally from the first energy bin³, i.e. close to the low energy threshold, we can roughly estimate, before doing any statistical analysis of the data, the shift of the allowed regions and constraints compared to the standard picture. For example, the expected rate of DM scatterings off Na nuclei is reduced by a factor $\sim 10^{-2}$ with respect to the standard case (see Fig. 2), and therefore the DAMA favored region, when assumed that most of the signal comes from DM scattering on Na, is shifted up by $\sim 10^2$ in the (m_χ, σ_p) plane. Taking now the DAMA-Na allowed region as benchmark, we can see how the other favorite regions and exclusion lines move with respect to it. CoGeNT moves a factor ~ 5 up, making the agreement with DAMA almost perfect. Concerning CRESST, the fit at small DM masses is due equally to O and Ca [10] in the standard scenario, from which we conclude that the cross section for DM magnetic dipole interaction with Ca is ~ 1.5 times bigger than that with O; the overall effect is an increase in σ_p , that lifts the favored region to better agree with DAMA and CoGeNT. In detail we expect that the CRESST allowed region moves a factor ~ 4 towards the DAMA-Na ballpark. Finally, CDMS and XENON move up by a factor ~ 6.5 and ~ 8.5 respectively, roughly irrespective of the choice of the threshold. This improves once again the agreement with the other experiments. For PICASSO the situation is different due to the special experimental setup in which the low energy threshold is a function of the temperature, and therefore one should be careful especially if the differential cross section is energy dependent. However, since the scattering in the PICASSO experiment is dominated by the dipole-dipole interaction which is of a contact type, a simple rescaling is again applicable, and we expect that the constraints will become a factor 2.5 more stringent (see left-panel of Fig. 2), compared to the standard picture.

3.2 Heavy Dark Matter

For higher DM masses, where for instance one can find the regions of the parameter space allowed by DAMA-I and CRESST-W, the effect of the long-range interaction turns to be very evident. As the minimal velocity for a given nuclear recoil v_{\min} becomes smaller than

²DAMA and CRESST are multi-target detectors and allowed regions at large DM mass correspond to scattering on I for DAMA and W for CRESST, while at small DM mass regions correspond to scattering on Na for DAMA and both O and Ca for CRESST.

³In CoGeNT, the larger part of the signal comes instead from the second energy bin.

v_E , the function $\zeta(v_{\min})$ changes behavior. For $v_{\min} \ll v_E$ (i.e. $m_\chi \gg m_N$)⁴

$$\frac{\mathcal{G}_{\text{SI}}(\eta_{\min}(E_R), t)}{\mathcal{I}(\eta_{\min}(E_R), t)} \simeq \left[1.8 v_0^2 - E_R \left(\frac{2m_N + m_\chi}{2m_N m_\chi} \right) \right]. \quad (30)$$

In this regime, for the nuclei whose interaction is SI, Θ scales as E_R^{-1} for the whole range of the recoil energies relevant for the direct detection experiments. If E_R increases sufficiently enough, v_{\min} becomes eventually larger than v_E and Θ assumes the constant behavior we described in the previous section. The difference in Θ between the low and high DM masses we depicted in Fig. (2) is that in the first case the plateau sets in at small recoil energies (smaller than the energy threshold of most experiments), whereas in the second case, the plateau sets in at large recoil energies (more than 25 keV). Instead for the other nuclei with large magnetic moment, the interaction is SD and as in the case of light DM the plateau manifests itself at low recoil energy.

Due to the pronounced energy dependence in this case, the allowed regions and the constraints will shift in the (m_χ, σ_p) plane considerably more than in the case of low DM mass (still compared to the standard contact spin-independent interaction). By taking again the DAMA-Na allowed region as a benchmark from the right panel of Fig. (2), we estimate that both DAMA-I and CRESST-W shift more than one order of magnitude up in σ_p . The same happens for CDMS and XENON. On the other hand PICASSO, like DAMA-Na, does not change its behavior respect to the light DM case: this is due to the fact that ^{19}F and ^{23}Na enjoy mostly spin-dependent interactions, that depend only slightly on the DM mass.

To summarize, taking into account the whole DM mass range, we see that, apart from an overall shift upwards in σ_p , there is a general trend of the various experiments to “gather”, getting closer to each other, with respect to the standard case. This behavior is not homogeneous in the DM mass and is more pronounced for masses above ~ 25 GeV. The effect is to favor a better fit compared to the standard case, with a better agreement of all the experiments. Even though this is true in general for any DM mass, we don’t expect anyway to get a good agreement for higher masses: in that region in fact the XENON experiment rules out the signal featured by other experiments by several orders of magnitude in the standard picture (Fig. 1), and the shifts that take place in our case are not big enough to change this situation.

Finally we comment on the dependence of the function Θ from the halo model considered, and in particular from the choice of the dispersion velocity v_0 . As we have seen, the transition between the two regimes discussed above is driven by the ratio v_{\min}/v_E , and it is only important for the nuclei which experience SI interactions with a DM particle. Therefore in this case we expect that for larger values of $v_E \approx v_0$, the plateau behavior of Θ sets in at higher recoil energies (or equivalently at smaller DM masses). This would make the shifts more pronounced even for light DM. In Sec. 5 and Figs. 3 and 4 we present the exact numerical results.

4 Data sets and analysis technique

In this section we discuss the techniques used to analyze the various data sets. In particular we adopt the approach of [57], and we summarize below the details of how we perform the

⁴This is generally true provided we consider a recoil energy E_R within our interest: from a minimum threshold value of a few keV up to 25 – 30 keV.

fits to data and constraints from null results experiments.

For DAMA, CoGeNT and CRESST, we test the null hypothesis (absence of signal on top of estimated background for CRESST and absence of modulation for DAMA and CoGeNT). From this we infer:

- i) the confidence level for the rejection of the null hypothesis (we find $8 \div 9\sigma$ for DAMA, $1 \div 2\sigma$ for CoGeNT, and 4σ for CRESST);
- ii) the domains in the relevant DM parameter space (defined by the DM mass m_χ and the DM magnetic dipole moment λ_χ) where the values of the likelihood function depart for more than $n\sigma$ from the null hypothesis, and thus the corresponding evidence of the DM signal. We use $n = 7, 8$, $n = 1$, and $n = 3, 4$ for DAMA, CoGeNT, and CRESST, respectively [7].

Our statistical estimator is the likelihood function of detecting the observed number of events $\mathcal{L} = \prod_i \mathcal{L}_i$, where the index i indicates the i -th energy bin in DAMA and CoGeNT, and the i -th detector in CRESST. For DAMA and CoGeNT \mathcal{L}_i are taken to follow a Gaussian distribution and for CRESST, since in this case the number of events in each sub-detector is low, a Poissonian one. Defining \mathcal{L}_{bg} as the likelihood of absence of signal, we assume the function $\tilde{y} = -2 \ln \mathcal{L}_{\text{bg}}/\mathcal{L}$ to be distributed as a χ^2 -variable with one degree of freedom for a given value of the DM mass (notice that for DAMA and CoGeNT \tilde{y} reduces to $\tilde{y} = \chi_{\text{bg}}^2 - \chi^2$). From the \tilde{y} function, the interval on λ_χ where the null hypothesis (i.e. $\lambda_\chi = 0$) can be excluded at the chosen level of confidence are extracted: 7σ (outer region) or 8σ (inner region) for DAMA, 1σ for CoGeNT and 3σ (outer region), 4σ (inner region) for CRESST. We then plot allowed regions in the (m_χ, λ_χ) plane.

We derive constraints from CDMS and XENON100 with a similar likelihood function $\lambda = -2 \ln \mathcal{L}/\mathcal{L}_{\text{bg}}$; here \mathcal{L} is the likelihood of detecting the observed number of events (2 for CDMS and 3 for XENON100), while in \mathcal{L}_{bg} the DM signal is not included. Both likelihoods are taken as Poissonian variables and λ is assumed to follow a χ^2 -distribution. For PICASSO we instead derive constraints by using a $\Delta\chi^2$ method of the data points shown in fig. 5 of [31]. Bounds are conservatively shown at 5σ C.L.

Concerning the experimental data sets and statistical methods, we refer to [57]; for completeness we summarize below for each experiment the most important ingredients used in the analysis.

- ◇ **DAMA**: We use the entire set of DAMA/NaI [4] and DAMA/LIBRA [5] data, corresponding to a cumulative exposure of 1.17 ton \times yr. We analyze the modulation amplitudes S_{mk}^{exp} reported in Fig. 6 of Ref. [5] requiring that the DM contribution to the unmodulated component of the rate, S_0 , does not exceed the corresponding experimental value S_0^{exp} in the 2 \div 4 keV energy range. We compute

$$y = -2 \ln \mathcal{L} \equiv \chi^2(\lambda_\chi, m_\chi) = \sum_{k=1}^8 \frac{(S_{mk} - S_{mk}^{\text{exp}})^2}{\sigma_k^2} + \frac{(S_0 - S_0^{\text{exp}})^2}{\sigma^2} \theta(S_0 - S_0^{\text{exp}}), \quad (31)$$

where σ_k and σ are the experimental errors on S_{mk}^{exp} and S_0^{exp} , respectively. The last term in Eq. (31) implements the upper bound on S_0 by penalizing the likelihood when S_0 exceeds S_0^{exp} with the Heaviside function θ . The detector energy resolution is parametrized by a Gaussian function of width $\sigma_{\text{res}}(E) = E(0.448/\sqrt{E} + 0.0091)$ [75],

using for the quenching factor the central values quoted by the collaboration, namely $q_{\text{Na}} = 0.3$ and $q_{\text{I}} = 0.09$ [76]. We don't take into account the possibility of a nonzero channeling fraction [35].

- ◇ **CoGeNT**: We consider the time-series of the data, treating the measured total rate as a constraint. Similarly to the analysis done on the DAMA data, we define

$$y = -2 \ln \mathcal{L} \equiv \chi^2(\lambda_\chi, m_\chi) = \sum_{k=1}^{16} \frac{(\tilde{S}_{m1,k} - \tilde{S}_{m1,k}^{\text{exp}})^2}{\sigma_k^2} + \sum_{k=1}^{16} \frac{(\tilde{S}_{m2,k} - \tilde{S}_{m2,k}^{\text{exp}})^2}{\sigma_k^2} + \sum_{j=1}^{31} \frac{(S_{0j} - S_{0j}^{\text{exp}})^2}{\sigma_j^2} \theta(S_{0j} - S_{0j}^{\text{exp}}); \quad (32)$$

here $\tilde{S}_{mk} = 1/\Delta t_k \int_{\Delta t_k} S_{mk} \cos[2\pi(t - \phi)/\tau] dt$, with Δt_k the temporal bin of the data, and $\tilde{S}_{mk}^{\text{exp}} = R_{mk}^{\text{exp}} - \langle R_{mk}^{\text{exp}} \rangle$, where R_{mk}^{exp} is the total rate (taken from Fig. 4 of Ref. [9]) and $\langle R_{mk}^{\text{exp}} \rangle$ is its annual average. The subscripts 1 and 2 in Eq. (32) refer to the first and second energy bins. The total rate in the $0.9 - 3.0$ keV_{ee} energy-bin is computed by subtracting the rate in the $0.5 - 0.9$ keV_{ee} bin to the rate in the $0.5 - 3.0$ keV_{ee} bin, with a Gaussian propagation of the errors. S_{0j}^{exp} and σ_j denote the experimental counts and the corresponding errors as given in Ref. [9] (31 energy bins in the interval $0.4 - 2$ keV_{ee}), after removal of the L-shell peaks but without removing any other background. The total fiducial mass is 330 g, the energy resolution is given by a Gaussian with width taken from [77], and the quenching factor below 10 keV is described by the relation $E = 0.2 E_R^{1.12}$ [78].

- ◇ **CRESST**: We compute the expected DM signal in each of the 8 CRESST detector modules. The acceptance regions and the number of observed events are provided in Table 1 of Ref. [10], and we derive background events according to estimates in Sec. 4 of Ref. [10]. A likelihood-ratio test yields a 4.1σ C.L. evidence for the best-fit of a DM signal over the background-only hypothesis, in good agreement with the result quoted by the collaboration. We use the published value of $730 \text{ kg} \times \text{days}$ for the exposure and assume an even contribution among the different modules⁵ (each module accounts therefore for an exposure of $730/8 \text{ kg} \times \text{days}$); we consider moreover a constant efficiency.
- ◇ **CDMS**: We use the “standard” 2009 CDMS-II results based on Ge data [29]; these are obtained employing conservative nuclear recoil selection cuts and assuming an energy threshold of 10 keV. The total exposure is $612 \text{ kg} \times \text{days}$ and we take the efficiency from the black curve of Fig. 5 in Ref. [79] with $q \simeq 1$ as quenching factor.⁶ In spite of an expected background of 0.9 ± 0.2 events, two signal events were found in the $10 - 100$ keV energy interval [29] (we use these numbers to derive the constraints).
- ◇ **XENON100**: We use the results presented in Ref. [30], with an exposure of 100.9 days in a fiducial volume of 48 kg. After all the cuts, three events were reported in the

⁵This is the same analysis performed in [57], although a value of $400/9 \text{ kg days}$ for the exposure was erroneously reported in the text of the published version.

⁶In the case of light DM, one can perform a similar analysis by using combined data from the CDMS and EDELWEISS experiments (see Fig. 1 in Ref. [80]), with basically the same results.

DM signal region in spite of an expected background of 1.8 ± 0.6 events. We model the data using a Poissonian distribution of photoelectrons, with a single-photoelectron resolution equal to 0.5. The shape of the \mathcal{L}_{eff} function is very crucial for such a low number of photoelectrons and for small DM masses. Following [57] we try to enclose a possible (but not exhaustive) uncertainty on the bounds derived for XENON100 by adopting two different approaches:

- i) we adopt as threshold the published value of 4 photoelectrons and the nominal central value of \mathcal{L}_{eff} as shown in Fig. 1 of Ref. [30], which relies heavily on linear extrapolation below $3 \text{ keV}_{\text{nr}}$;
- ii) more conservatively, we raise the threshold for the photomultipliers to 8 photoelectrons: this value is the lowest one for which the analysis is nearly independent on the shape of \mathcal{L}_{eff} below $3 \text{ keV}_{\text{nr}}$.

Notice that these two approaches are not exhaustive of all the possible assumptions one can do to determine the XENON100 response to light DM (for further discussion and considerations, see e.g. Refs. [32,33]). It appears therefore still preliminary, given these large uncertainties, to assume the bounds quoted by the collaboration as strictly firm. The 8 photoelectrons bound is less dependent on the \mathcal{L}_{eff} extrapolation, and therefore, conservatively, we consider it as more appropriate.

Finally, we follow Eqs. (13–16) in Ref. [81] to compute the expected signal. We derive upper bounds for both CDMS and XENON as mentioned at the beginning of this section.

- ◇ **PICASSO**: The PICASSO experiment, located at SNOLAB [31], is very different from the ones discussed above; it is in fact based on the superheated droplet technique, a variant of the bubble chamber technique, to search for DM recoiling on ^{19}F in a C_4F_{10} target. The experimental procedure consists in measuring the acoustic signal released by the nucleation of a bubble as a function of the temperature T . Details of the detector principle can be found in [82,83]. Since bubble formation is only triggered above a certain energy threshold $E_{\text{th}}(T)$, the spectrum of the particle-induced energy depositions can be constructed by varying the temperature. We compute the predicted DM rate as a function of $E_{\text{th}}(T)$ from Eq. (3) of [31] and we compare such prediction with the experimental rate shown in Fig. 5 by using a $\Delta\chi^2$ method. In this analysis we adopt two reference values of the parameter $a(T)$ which describes the steepness of the energy threshold; namely we take $a = (2.5, 7.5)$ in order to encapsulate as much as possible the experimental uncertainties [31]. We checked our result against the one of the collaboration given in Fig. 7 of Ref. [31], and we found an excellent agreement. Remaining coherent with our choice of being conservative we show here the result at 5σ , as we did also for the other exclusion experiments.

5 Fit to the direct detection experiments

We analyze the direct detection data sets by using a standard isothermal halo model, which basically implies a truncated Maxwell-Boltzmann velocity distribution function (see discussion in Sec. 2.3). Since the response of direct detection experiments is quite sensitive to the DM distribution in the galactic halo [6], especially in the scenario we are interested to study,

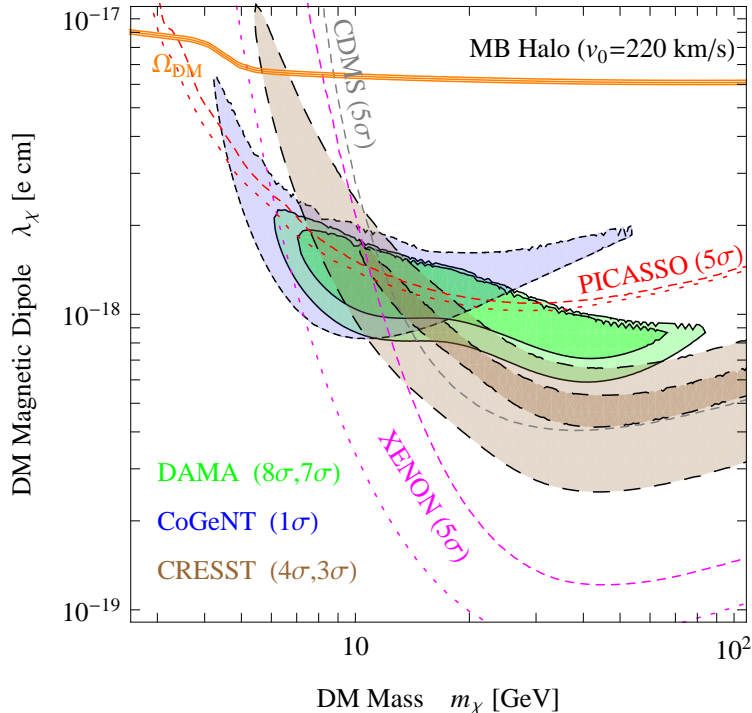


Figure 3: DM magnetic dipole moment λ_χ as a function of the Dark Matter mass m_χ . The galactic halo has been assumed in the form of an isothermal sphere with velocity dispersion $v_0 = 220$ km/s and local density $\rho_0 = 0.3$ GeV/cm³. Notations are the same as in Fig. 1; to match the two figures, one has to note that the role of σ_p is played here by $\alpha\lambda_\chi^2$. The orange strip shows the values for (m_χ, λ_χ) that fit the relic abundance Ω_{DM} assuming a completely thermal DM production (see Sec. 6).

we take into account uncertainties on the velocity dispersion v_0 , as discussed in Ref. [6]. We will use the three values $v_0 = 170, 220, 270$ km/s, which bracket the uncertainty in the local rotational velocity. Let us notice that the value of the local DM density ρ_0 is correlated to the adopted value of v_0 , as discussed e.g. in Ref. [6]. This corresponds to the model denoted as A0 in [6], and we adopt here the case of minimal halo, which implies lower values of the local DM density (since a fraction of the galactic potential is supported by the disk/bulge). In turn, this implies the adoption of $\rho_0 = 0.18, 0.30, 0.45$ GeV/cm³ for $v_0 = 170, 220, 270$ km/s, respectively [6].

Fig. 3 shows the constraints and the favored regions coming from DM direct detection experiments in the (m_χ, λ_χ) plane. The galactic halo has been assumed to be in the form of an isothermal sphere with velocity dispersion $v_0 = 220$ km/s and local density $\rho_0 = 0.3$ GeV/cm³. The solid green contours denote the regions compatible with the DAMA annual modulation effect [4, 5], in absence of channeling [35]. The short-dashed blue contour refers to the region derived from the CoGeNT annual modulation signal [9], when the bound from the unmodulated CoGeNT data is taken into account. The dashed brown contours denote the regions compatible with the CRESST excess [10]. For all the data sets, the contours refer to regions where the absence of modulation can be excluded with a C.L. of 7σ (outer region), 8σ (inner region) for DAMA, 1σ for CoGeNT, and the absence of an excess can be excluded at 3σ (outer region), 4σ (inner region) for CRESST. Constraints derived by the null result

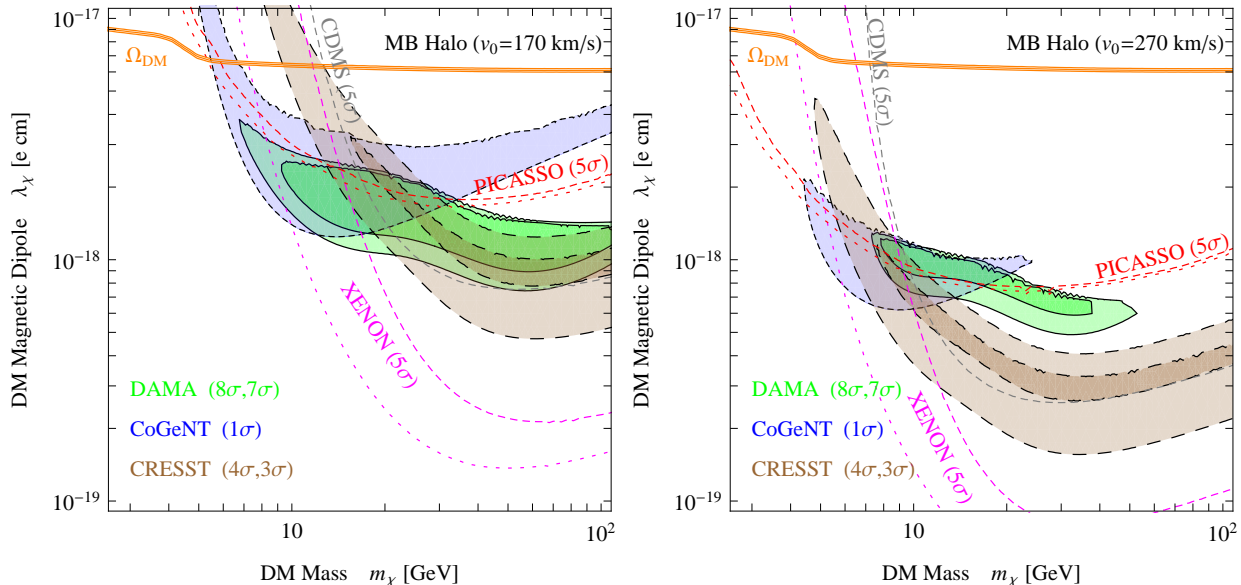


Figure 4: DM magnetic dipole moment λ_χ as a function of the Dark Matter mass m_χ . The galactic halo has been assumed in the form of an isothermal sphere with velocity dispersion $v_0 = 170$ km/s and local density $\rho_0 = 0.18$ GeV/cm³ (left panel); $v_0 = 270$ km/s and local density $\rho_0 = 0.45$ GeV/cm³ (right panel). Notations are the same as in Fig. 1; to match the two figures, one has to note that the role of σ_p is played here by $\alpha\lambda_\chi^2$. The orange strip shows the values for (m_χ, λ_χ) that fit the relic abundance Ω_{DM} , in the assumption of thermal DM production (see Sec. 6).

experiments are shown at 5σ as gray, magenta and red dashed lines for CDMS, XENON100 and PICASSO respectively. For the XENON detector, as discussed in the previous section, the constraints refer to thresholds of 4 and 8 photoelectrons, while for PICASSO we take into account the uncertainty in the intrinsic energy resolution of the employed detection technique [31].

We can see that, as expected from the discussion in Sec. 3, for a given value of m_χ , all the experiments determine a DM-proton cross section $\sigma_p = \alpha\lambda_\chi^2$ that is higher than the one for the standard case of non isospin violating contact interaction depicted in Fig. 1; to give a benchmark value, DAMA points now to $\sigma_p \sim 1.5 \times 10^{-38}$ cm², about 10^2 times above the standard case, as shown in Sec. 3. Moreover we observe the expected gathering of the various experiments, that get closer to each other with respect to the standard scenario, for an overall better agreement, and with DAMA, CoGeNT and CRESST featuring a larger overlap at low masses. Both the DAMA and CoGeNT regions point towards a DM mass in the 10 GeV ballpark (more specifically, from about 7 up to about 12 GeV) and DM magnetic dipole moment around 1.5×10^{-18} e cm without exceeding the constraints, corresponding to an inverse mass energy scale of circa $\Lambda_M \sim 10$ TeV. CRESST allows for even heavier DM masses, but still compatible with the range determined by the other two experiments. CDMS and XENON, on the other hand, exclude a smaller part of the parameter space with respect to the standard case. These two experiments do not exclude the overlapping region once one accepts our conservative choice of the XENON threshold at 8 photoelectrons. At 5σ it is seen that PICASSO cannot exclude the common regions of the experiments reporting a signal. Finally, we also notice the occurrence of the expected flattening of the various experiments,

meaning that the tilt featured in the standard case (higher mass regions pointing to lower σ_p) is very suppressed in the case of magnetic moment interaction, as explained in Sec. 3.

These results depend on the galactic halo model assumed. The effect induced by the variation in the DM dispersion velocity is shown in the two panels of Fig. 4. In the case of $v_0 = 170$ km/s, the regions are not significantly modified as compared to the case $v_0 = 220$ km/s, except for the overall normalization due to the different values of the local DM density in the two cases. Larger dispersion velocities, instead, lead to the second regime discussed in Sec. 3 also at small DM masses (see right panel of Fig. 2). Due to the high energy dependence of the differential rate in this regime, experiments that use heavy targets and/or have high thresholds, get a suppression of the event rate, and point therefore to relatively higher values of the interaction cross section compared to the standard case. Since the DM signal is expected at lower recoil energies, smaller DM masses are now favorite. The right panel of Fig. 4 shows in fact that the allowed regions are shifted toward smaller DM masses for $v_0 = 270$ km/s.

6 Relic Abundance

In addition to a satisfactory fitting of the direct detection data, the DM magnetic dipole interaction can accommodate the annihilation cross section appropriate for thermal production. Since it couples to the photon, the DM annihilates to any charged Standard Model particle-antiparticle pair, with mass lower than m_χ . Considering a DM particle with 10 GeV mass, that as we argued fits well the direct detection experiments, the allowed primary channels are e^+e^- , $\mu^+\mu^-$, $\tau^+\tau^-$, $u\bar{u}$, $d\bar{d}$, $s\bar{s}$, $c\bar{c}$, $b\bar{b}$ and $\gamma\gamma$.

The DM annihilation cross sections to Standard Model fermions and photons at tree level are

$$\sigma_{\chi\bar{\chi}\rightarrow f\bar{f}}(s) = \frac{\alpha Q_f^2 N_C^f \beta_f}{12} \frac{1}{\beta_\chi s^2} \times \left[\lambda_\chi^2 (s^2(3 - \beta^2) + 12m_\chi^2 s + 48m_f^2 m_\chi^2) + d_\chi^2 (s^2(3 - \beta^2) - 12m_\chi^2 s) \right], \quad (33)$$

$$\sigma_{\chi\bar{\chi}\rightarrow\gamma\gamma}(s) = \frac{\lambda_\chi^4}{4\pi\beta_\chi} \left(m_\chi^2 + \frac{s}{8} - \frac{s\beta_\chi^2}{24} - 4\frac{m_\chi^4}{s} \frac{\text{arcth}(\beta_\chi)}{\beta_\chi} \right), \quad (34)$$

where $\beta_{\chi,f} = (1 - 4m_{\chi,f}^2/s)^{1/2}$, $\beta \equiv \beta_\chi\beta_f$, Q_f is the charge of the fermion and finally $N_C^\ell = 1$ for leptons and $N_C^q = 3$ for quarks. In the non-relativistic limit, Eqs. (33) and (34) reduce to

$$\langle \sigma_{\chi\bar{\chi}\rightarrow f\bar{f}} v_{\text{rel}} \rangle \simeq N \alpha \lambda_\chi^2 \cdot \text{BR}(f), \quad (35)$$

$$\langle \sigma_{\chi\bar{\chi}\rightarrow\gamma\gamma} v_{\text{rel}} \rangle \simeq \frac{1}{4\pi} \lambda_\chi^4 m_\chi^2, \quad (36)$$

where $N = \sum_f Q_f^2 N_C^f = 20/3$ accounts for the number of degrees of freedom of the Standard Model fermions into which the DM can annihilate; the branching ratios $\text{BR}(f)$ are defined as $\text{BR}(f) = Q_f^2 N_C^f / N$. As one can see, for the low values of $\lambda_\chi m_\chi$ pointed by the direct detection experiments, the two photons final state is suppressed with respect to the fermionic one. Using a DM energy density $\Omega_{\text{DM}} h^2 = 0.1126 \pm 0.0036$ measured by WMAP [84], we

show⁷ with an orange strip in the (m_χ, λ_χ) plane of Figs. 3 and 4 the phase space where a thermal production of the magnetic DM is possible.

It can be seen in Figs. 3 and 4 that the agreement between the allowed regions and the relic abundance depends strongly on the dispersion velocity v_0 . The best agreement takes place for lower values of v_0 . This is due to the fact that, as commented already in Sec. 5, ρ_0 is linked to the dispersion velocity v_0 . By varying v_0 , ρ_0 is modified accordingly, changing therefore the expected rate and the fitting values for the interaction cross sections, or in other words λ_χ . As a consequence, the favored regions and constraint lines of direct detection experiments move along the vertical axis in the (m_χ, λ_χ) plane. For lower velocity dispersion, both the local DM density and the expected rate decrease. Therefore, the favored regions will point to a higher DM magnetic moment, getting closer to the relic abundance strip. The value of the relic abundance is obviously independent on the local DM density.

The fact that the magnetic DM (with only two parameters) provides a good fit to the direct detection experiments and simultaneously can accommodate a thermal annihilation cross section (which is several orders of magnitude stronger than the DM-nucleon cross section in the context of “standard” contact interaction) is not easily met by other DM candidates. Although there are candidates that can have a DM-nucleon cross section much lower than their thermal annihilation cross section, these candidates have usually spin-dependent interactions and cannot fit nicely the direct search experiments with a positive DM signal. For a typical candidate with spin-independent contact interactions, and for a strength of interaction that leads to a DM-nucleon cross section pointed by the direct detection experiments featuring a signal, the annihilation cross section is way too small to produce this candidate thermally. In order to match, a suppression mechanism for the direct detection event rate should take place. In the case of magnetic moment DM, this mechanism exists and has two different reasons for the SI and the SD parts of the interaction. As already explained in Sec. 3, this suppression is encoded into the function Θ in Eq. (26), that spans roughly from 10^{-3} to 10^{-1} for a 10 GeV DM (see Fig. 2). This suppression is a result between two competing factors for the SI case: the enhancement provided by the E_R^{-1} dependence of the differential cross section, and the suppression provided by the kinetic integral; in the SD case, the suppression is instead due to the lack of the A^2 enhancement usually present in the standard SI case.

Notice that in the case of electric dipole DM one faces a very different situation: here the differential cross section has the same dependence on the velocity as in a contact interaction (Eq. (7)), and therefore there is no kinetic suppression, while on the contrary the rate is enhanced by the E_R^{-1} dependence. Moreover, the annihilation to fermions is a p-wave process, Eq. (33), and therefore the annihilation cross section is suppressed, making the value of d_χ needed to fit the relic abundance even bigger.

Furthermore, it is worth to point out that neither asymmetric/mixed DM [86], nor oscillating DM [87–89] can improve the agreement between the relic density and the allowed regions of direct DM searches in the context of magnetic DM interaction.

⁷The figures are produced by solving numerically the Boltzmann equation

$$\dot{n}_{\text{tot}} + 3Hn_{\text{tot}} = -\frac{1}{2}\langle\sigma_{\text{ann}}v_{\text{rel}}\rangle(n_{\text{tot}}^2 - n_{\text{eq}}^2), \quad (37)$$

where n_{tot} is the total number density of particles and antiparticles, H is the Hubble parameter and for $\langle\sigma_{\text{ann}}v_{\text{rel}}\rangle$ we use the more precise formula given in Eq. (3.8) of [85].

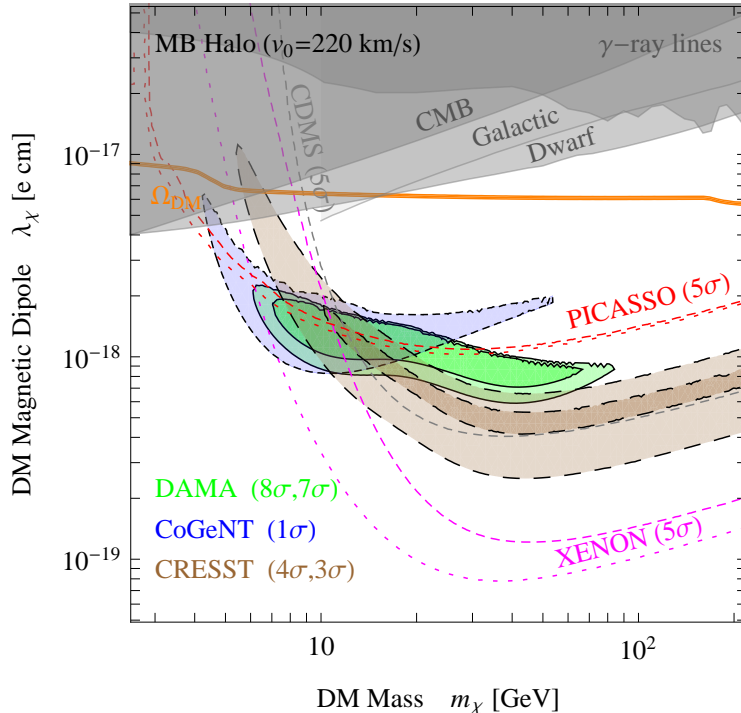


Figure 5: DM magnetic dipole moment λ_χ as a function of the Dark Matter mass m_χ . The galactic halo has been assumed in the form of an isothermal sphere with velocity dispersion $v_0 = 220$ km/s and local density $\rho_0 = 0.3$ GeV/cm³. Notations are the same as in Fig. 1. The orange strip shows the values for (m_χ, λ_χ) that fit the relic abundance Ω_{DM} , in the assumption of thermal DM production (see Sec. 6). The shaded regions refer to the constraints from γ -ray lines, CMB, galactic γ -rays and dwarf galaxies. These constraints are only valid in the assumption of symmetric DM. The galactic photons constraint enforces total annihilation of the DM into $b\bar{b}$, and therefore a less stringent constraint is expected for magnetic moment DM.

7 Constraints

Given the qualitative agreement between the direct detection allowed regions and the fit of the relic abundance, it is natural to ask whether constraints coming from other searches could limit the parameter space of the magnetic moment DM. This is even more pressing since the bounds coming from indirect DM searches are on the verge of constraining the thermal annihilation rate for light DM particles. We will discuss the constraints imposed by indirect searches, colliders and by the observations of compact stars, and then identify the most stringent ones.

7.1 Epoch of reionization and CMB

Strong constraints are imposed on DM annihilations from considering the effect on the generation of the CMB anisotropies at the epoch of recombination (at redshift ~ 1100) and their subsequent evolution down to the epoch of reionization. The actual physical effect of energy injection around the recombination epoch results in an increased amount of free

electrons, which survive to lower redshifts and affect the CMB anisotropies [90–93]. Detailed constraints have been recently derived in [94,95], based on the WMAP (7-year) and Atacama Cosmology Telescope 2008 data. The constraints are somewhat sensitive to the dominant DM annihilation channel: annihilation modes for which a portion of the energy is carried away by neutrinos or stored in protons have a smaller impact on the CMB; on the contrary the annihilation mode which produces directly e^+e^- is the most effective one. Usually the approach here is to consider 100% annihilation rate in a single final state; anyway, in our case several annihilation channels are open, and therefore we expect a smaller energy injection in the interstellar medium with respect to the case of annihilation only into e^+e^- . In Fig. 5 we reproduce the constraints as obtained in Refs. [93–95] considering now all the channels, each with its branching ratio defined in Sec. 6.

7.2 Present epoch γ -rays

For most of the DM annihilation modes, another relevant constraint is in fact imposed by the indirect DM searches in the present epoch. The DM constraints provided by the FERMI-LAT γ -ray data are particularly relevant as they are now cutting into the thermal annihilation cross section for low DM masses ($\lesssim 30$ GeV) and a variety of channels.

In particular, dwarf satellite galaxies of the Milky Way are among the most promising targets for Dark Matter searches in γ -rays because of their large dynamical mass to light ratio and small expected background from astrophysical sources. No dwarf galaxy has been detected in γ -rays so far and stringent upper limits are placed on DM annihilation by applying a joint likelihood analysis to 10 satellite galaxies with 2 years of FERMI-LAT data, taking into account the uncertainty in the Dark Matter distribution in the satellites [96]. The limits are particularly strong for hadronic annihilation channels, and somewhat weaker for leptonic channels as diffusion of leptons out of these systems is poorly constrained. In our case, having both hadronic as well as leptonic annihilation channels, we expect again a weaker constraint with respect to the pure hadronic annihilation (see e.g. figure 2 in Ref. [96]).

Other strong limits on annihilation channels are set by, for example, the γ -ray diffuse emission measurement at intermediate latitudes, which probes DM annihilation in our Milky Way halo [97–99]. In particular, the most recent limits come from 2 years of the FERMI-LAT data in the $5^\circ \leq b \leq 15^\circ$, $-80^\circ \leq \ell \leq 80^\circ$ region [99], where b and ℓ are the galactic latitude and longitude. Since bounds on all annihilation channels are not available with the latest data, we report only the most stringent one, coming from $b\bar{b}$.

The last kind of constraints that we can set on DM annihilation in the case of magnetic moment interaction comes from γ -ray lines. Indeed, given the possibility of annihilation in two photons, we expect a line in the cosmic photon spectrum at energies equal to the mass of the DM. Constraints on the annihilation cross section into photons can be drawn from the latest FERMI-LAT data [100]. For instance, the FERMI-LAT collaboration excludes at 95% the annihilation $\langle \sigma_{\chi\bar{\chi} \rightarrow f\bar{f}} v_{\text{rel}} \rangle < 0.5 \times 10^{-27} \text{ cm}^3/\text{s}$ for a DM mass $m_\chi = 30$ GeV in the case of an isothermal halo. In our case we use the latest (preliminary) data on the flux from spectral lines (shown in slide 39 of [101]) to constrain the annihilation cross section of Eq. (36)⁸. We consider an all-sky region with the Galactic plane removed ($|b| > 10^\circ$), plus a $20^\circ \times 20^\circ$ square region centered on the Galactic center [100]. Notice that, for small DM masses and dipole moments, the one-loop contribution becomes comparable with the tree

⁸A similar study has been published in Ref. [102] for DM masses above 30 GeV.

level one; a rough estimate of the loop cross section in the non-relativistic limit is $\alpha^3 \lambda_\chi^2 / 4\pi$, and therefore we expect it to become sizeable for $\lambda_\chi m_\chi < \alpha^{3/2} \simeq 6 \times 10^{-4}$. In the part of the parameter space probed by γ -ray lines searches the loop correction is negligible.

We superimpose all these constraints in Fig. 5. We see that, apart from the γ lines bound, they are somewhat stronger than the CMB one considered above. We keep however the latter as it is less model dependent.

As shown in Fig. 4, a change in the DM local density modifies the direct searches results. This does not happen for indirect searches, as they are not very sensitive to ρ_0 . Therefore the constraints shown in Fig. 5 also apply, unchanged, to this case. For lower DM dispersion velocity v_0 these constraints start to play an important role in cutting the parameter space for direct detection searches.

7.3 Collider and other Astrophysical constraints

The constraints we have addressed above apply to the case of symmetric (thermally produced) DM. These constraints are not relevant in the case where DM is of asymmetric nature. There are two extra type of constraints: constraints imposed by collider searches, and constraints imposed by observations of compact stars such as white dwarfs and neutron stars. The collider constraints are applicable whether DM is symmetric or not, whereas the compact star constraints are valid only for asymmetric DM.

The collider constraints emerge from the fact that for a given λ_χ and m_χ that fit the direct DM searches experimental data (and even provide the proper DM annihilation cross section for thermal production), the cross section for production of a pair of DM particles in colliders is completely fixed. The processes that lead to constraints are mono-photon production (from initial or final state) plus missing energy due to the pair of DM particles in e^+e^- collisions at LEP, or mono-jet production plus missing energy in proton-antiproton collision in Tevatron, or proton-proton collisions at LHC. In the case of magnetic DM these constraints have been studied in [48, 49] where it is found that the upper bound on λ_χ is safely above the range of values of λ_χ relevant for the direct search experiments (for the range of $m_\chi \sim 10$ GeV).

In the case of asymmetric DM, constraints can be imposed by compact star observations based on the fact that a substantial number of captured DM particles might lead to gravitational collapse and formation of a black hole that can destroy the host star. The magnetic DM being a fermion evades the severe constraints on asymmetric bosonic DM based on neutron stars [103–105]. The constraints on self-DM cross section with Yukawa interactions presented in [106] are avoided for several reasons: firstly DM-DM interactions scale as $m_\chi^2 \lambda_\chi^4$ (leading to a typical DM-DM cross section of $\sim 10^{-43}$ cm² which is much smaller than the constraint). Secondly the constraints are not directly applicable because the mediator of the magnetic DM is a massless photon (and not a massive mediator necessary for the constraint) and the DM-DM interaction is repulsive. The latter adds up to the effect of the Fermi pressure of the DM particles and therefore the amount of particles needed for gravitational collapse cannot be accumulated within the age of the Universe. A potential attractive photon interaction takes place in the symmetric case, which will however lead also to annihilation of the DM population inside the neutron star invalidating thus the constraint derived from black hole formation.

Finally the magnetic DM evades constraints on the spin-dependent part of the cross section imposed by observations of white dwarfs [107]. Although these constraints are typically weaker than the ones derived from direct searches at the range $m_\chi \sim 10$ GeV, they could become stricter if spin-dependent interactions scale as some (positive) power of the recoil energy. Since DM particles acquire high velocities when entering the white dwarf, such constraints could in principle exclude such a candidate. However, as it was pointed out in [41], the spin-dependent cross section does not scale with the recoil energy and therefore the white dwarf constraints can be safely ignored.

8 Conclusions

We investigated a fermionic Dark Matter particle carrying magnetic dipole moment and analyzed its impact on direct detection experiments. We provided an analytic understanding of how the photon induced long-range interaction neatly modifies the experimental allowed regions with respect to the typically assumed contact interaction. We showed that this candidate can accommodate the DAMA, CoGeNT and CRESST experimental results. By assuming conservative bounds we have demonstrated that this candidate is not ruled out by the CDMS, XENON and PICASSO experiments. Assuming a symmetric Dark Matter sector, we also determined the associated thermal relic density and provided relevant bounds from indirect search experiments. We found that all the experimental results are compatible with a Dark Matter particle with mass around 10 GeV and magnetic moment 1.5×10^{-18} e cm, which corresponds to a new physics scale $\Lambda_M \sim 10$ TeV.

Acknowledgments. We thank Robert Foot, Aldo Morselli and Kimmo Kainulainen for useful discussions. We are particularly grateful to Marco Regis for sharing parts of the code used for the data analysis.

A Appendix

In this appendix we estimate the effect of the dipole-dipole interaction term in Eq. (6) for all the targets considered in our analysis. To this aim, one can define the useful ratio

$$r(E_R) \equiv \frac{dR_{\text{SD}}}{dE_R} \cdot \left(\frac{dR_{\text{SI}}}{dE_R} \right)^{-1} = \frac{\int d\sigma_{\text{SD}}/dE_R v dn_\chi}{\int d\sigma_{\text{SI}}/dE_R v dn_\chi}, \quad (38)$$

which measures the main contribution of the total recoil rate for a given nuclear specie in a detector. If $r > 1$ the interaction is largely spin-dependent, while it is mostly spin-independent for $r < 1$.

For elastic DM, which features $\delta = 0$, the ratio r can be computed from Eqs. (27) and (28), yielding

$$r(E_R) = \frac{2}{3} \Theta_{\text{SI}}(E_R)^{-1} \left(\frac{1}{A} \frac{\bar{\lambda}_{\text{nuc}} \mu_{\chi n}}{\lambda_p m_p} \right)^2, \quad (39)$$

where for the illustrative purposes of this appendix we approximated here $F_{\text{SI}}(E_R) \simeq F_{\text{SD}}(E_R)$. In Fig. 6 we show the ratio r as a function of the nuclear recoil energy considering a DM mass of 10 GeV, which gives a good combined fit to the existing experiments, and 50 GeV, for a comparison. One can see that the dipole-dipole term plays a major role

for DAMA (Na, I) and PICASSO (F), while being negligible for all the other experiments considered, as stated in the main text.

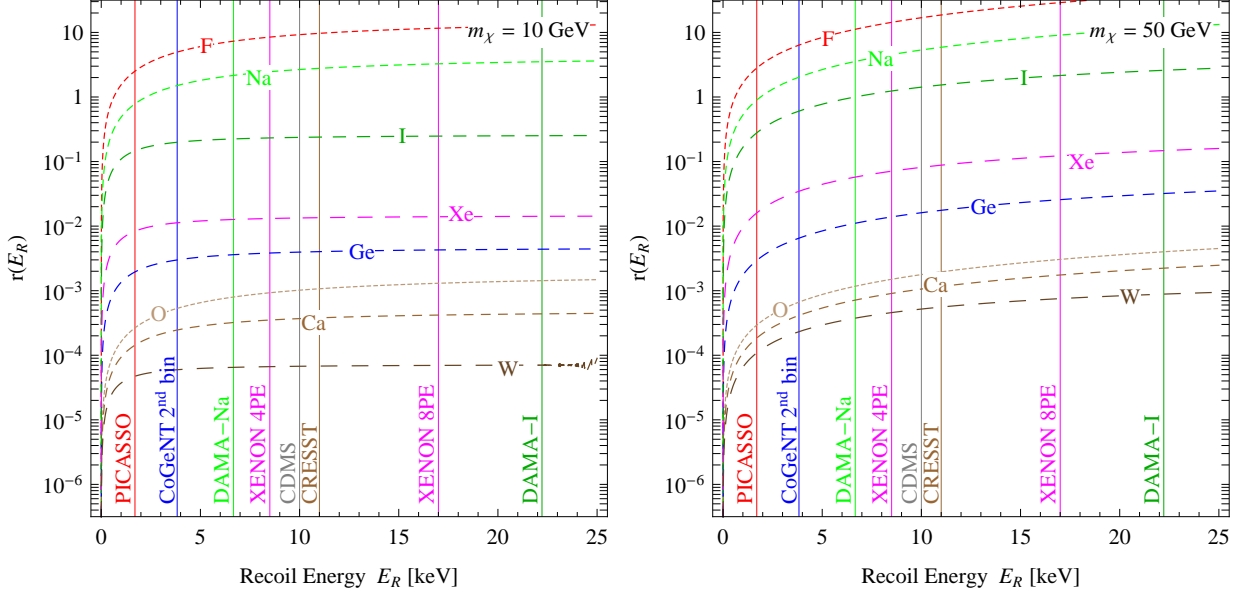


Figure 6: The SD to SI rates ratio r defined in Eq. (38) for the two cases of $m_\chi = 10$ GeV (left) and $m_\chi = 50$ GeV (right). We consider here a Maxwellian halo with local dispersion velocity 220 km/s. Supposing the major part of the signal to come from the lower energy threshold (or from the second bin in the case of CoGeNT), r can be determined in the figure by the point where the dashed line meets the vertical line with the same color, for each nuclear element.

While the dipole-charge interaction already provides a good fit, the effect of the dipole-dipole interaction contributes to a better agreement between the experiments. In fact, the increase in the cross section in DAMA favors a lower value for the DM magnetic moment λ_χ , and therefore the DAMA region shifts down towards CoGeNT and CRESST. The overlap becomes then almost perfect, for a Maxwellian velocity distribution, especially with velocity dispersion 220 km/s. On the other hand also the bound by PICASSO lowers, but even this enhanced constraint excludes only a minor part of the overlap zone.

References

- [1] R. Bernabei, P. Belli, F. Montecchia, W. Di Nicolantonio, A. Incicchitti, D. Prospero, C. Bacci and C. J. Dai *et al.*, Phys. Lett. B **424** (1998) 195.
- [2] A. K. Drukier, K. Freese and D. N. Spergel, Phys. Rev. D **33** (1986) 3495.
- [3] K. Freese, J. A. Frieman and A. Gould, Phys. Rev. D **37** (1988) 3388.
- [4] R. Bernabei *et al.* [DAMA Collaboration], Eur. Phys. J. C **56** (2008) 333 [[arXiv:0804.2741](#) [astro-ph]].
- [5] R. Bernabei, P. Belli, F. Cappella, R. Cerulli, C. J. Dai, A. d'Angelo, H. L. He and A. Incicchitti *et al.*, Eur. Phys. J. C **67** (2010) 39 [[arXiv:1002.1028](#) [astro-ph.GA]].
- [6] P. Belli, R. Cerulli, N. Fornengo and S. Scopel, Phys. Rev. D **66** (2002) 043503 [[hep-ph/0203242](#)].
- [7] P. Belli, R. Bernabei, A. Bottino, F. Cappella, R. Cerulli, N. Fornengo and S. Scopel, Phys. Rev. D **84** (2011) 055014 [[arXiv:1106.4667](#) [hep-ph]].
- [8] C. E. Aalseth *et al.* [CoGeNT Collaboration], Phys. Rev. Lett. **106** (2011) 131301 [[arXiv:1002.4703](#) [astro-ph.CO]].
- [9] C. E. Aalseth, P. S. Barbeau, J. Colaresi, J. I. Collar, J. Diaz Leon, J. E. Fast, and N. Fields *et al.*, Phys. Rev. Lett. **107** (2011) 141301 [[arXiv:1106.0650](#) [astro-ph.CO]].
- [10] G. Angloher, M. Bauer, I. Bavykina, A. Bento, C. Bucci, C. Ciemniak, G. Deuter and F. von Feilitzsch *et al.*, [arXiv:1109.0702](#) [astro-ph.CO].
- [11] R. Foot, Phys. Lett. B **703** (2011) 7 [[arXiv:1106.2688](#) [hep-ph]].
- [12] T. Schwetz, J. Zupan, JCAP **1108** (2011) 008. [[arXiv:1106.6241](#) [hep-ph]].
- [13] M. Farina, D. Pappadopulo, A. Strumia and T. Volansky, JCAP **1111** (2011) 010 [[arXiv:1107.0715](#) [hep-ph]].
- [14] C. McCabe, Phys. Rev. D **84** (2011) 043525 [[arXiv:1107.0741](#) [hep-ph]].
- [15] P. J. Fox, J. Kopp, M. Lisanti, N. Weiner, [[arXiv:1107.0717](#) [hep-ph]].
- [16] D. Hooper and C. Kelso, Phys. Rev. D **84** (2011) 083001 [[arXiv:1106.1066](#) [hep-ph]].
- [17] P. Gondolo, P. Ko and Y. Omura, Phys. Rev. D **85** (2012) 035022 [[arXiv:1106.0885](#) [hep-ph]].
- [18] E. Del Nobile, C. Kouvaris, F. Sannino, Phys. Rev. **D84** (2011) 027301. [[arXiv:1105.5431](#) [hep-ph]].
- [19] C. Arina, J. Hamann and Y. Y. Y. Wong, JCAP **1109** (2011) 022 [[arXiv:1105.5121](#) [hep-ph]].
- [20] M. T. Frandsen, F. Kahlhoefer, J. March-Russell, C. McCabe, M. McCullough, K. Schmidt-Hoberg, [[arXiv:1105.3734](#) [hep-ph]].

- [21] D. E. Kaplan, G. Z. Krnjaic, K. R. Rehermann and C. M. Wells, [arXiv:1105.2073](#) [hep-ph].
- [22] J. L. Feng, J. Kumar, D. Marfatia and D. Sanford, Phys. Lett. B **703** (2011) 124 [[arXiv:1102.4331](#) [hep-ph]].
- [23] A. L. Fitzpatrick and K. M. Zurek, Phys. Rev. D **82** (2010) 075004 [[arXiv:1007.5325](#) [hep-ph]].
- [24] D. Hooper, J. I. Collar, J. Hall, D. McKinsey and C. Kelso, Phys. Rev. D **82** (2010) 123509 [[arXiv:1007.1005](#) [hep-ph]].
- [25] R. Foot, Phys. Lett. B **692** (2010) 65 [[arXiv:1004.1424](#) [hep-ph]].
- [26] S. Chang, J. Liu, A. Pierce, N. Weiner and I. Yavin, JCAP **1008** (2010) 018 [[arXiv:1004.0697](#) [hep-ph]].
- [27] A. L. Fitzpatrick, D. Hooper and K. M. Zurek, Phys. Rev. D **81** (2010) 115005 [[arXiv:1003.0014](#) [hep-ph]].
- [28] J. Kopp, T. Schwetz and J. Zupan, JCAP **1002** (2010) 014 [updated version in [arXiv:0912.4264](#) [hep-ph]].
- [29] Z. Ahmed *et al.* [CDMS-II Collaboration], Science **327**, (2010), 1619-1621. [[arXiv:0912.3592](#) [astro-ph.CO]].
- [30] E. Aprile *et al.* [XENON100 Collaboration], Phys. Rev. Lett. **107** (2011) 131302 [[arXiv:1104.2549](#) [astro-ph.CO]].
- [31] S. Archambault *et al.* [PICASSO Collaboration], [arXiv:1202.1240](#) [hep-ex].
- [32] R. Bernabei, P. Belli, A. Incicchitti and D. Prosperi, [arXiv:0806.0011](#) [astro-ph].
- [33] J. I. Collar, [arXiv:1106.0653](#) [astro-ph.CO].
- [34] J. I. Collar, [arXiv:1103.3481](#) [astro-ph.CO].
- [35] R. Bernabei, P. Belli, F. Montecchia, F. Nozzoli, F. Cappella, A. Incicchitti, D. Prosperi and R. Cerulli *et al.*, Eur. Phys. J. C **53** (2008) 205 [[arXiv:0710.0288](#) [astro-ph]].
- [36] N. Bozorgnia, G. B. Gelmini and P. Gondolo, JCAP **1011** (2010) 019 [[arXiv:1006.3110](#) [astro-ph.CO]].
- [37] B. Feldstein, A. L. Fitzpatrick, E. Katz and B. Tweedie, JCAP **1003** (2010) 029 [[arXiv:0910.0007](#) [hep-ph]].
- [38] J. Bagnasco, M. Dine and S. D. Thomas, Phys. Lett. B **320**, 99 (1994) [[hep-ph/9310290](#)].
- [39] M. Pospelov and T. ter Veldhuis, Phys. Lett. B **480** (2000) 181 [[hep-ph/0003010](#)].
- [40] K. Sigurdson, M. Doran, A. Kurylov, R. R. Caldwell and M. Kamionkowski, Phys. Rev. D **70** (2004) 083501 [Erratum-ibid. D **73** (2006) 089903] [[astro-ph/0406355](#)].

- [41] V. Barger, W. -Y. Keung and D. Marfatia, Phys. Lett. B **696**, 74 (2011) [[arXiv:1007.4345](#) [hep-ph]].
- [42] S. Chang, N. Weiner and I. Yavin, Phys. Rev. D **82** (2010) 125011 [[arXiv:1007.4200](#) [hep-ph]].
- [43] W. S. Cho, J. -H. Huh, I. -W. Kim, J. E. Kim and B. Kyaee, Phys. Lett. B **687** (2010) 6 [Erratum-ibid. B **694** (2011) 496] [[arXiv:1001.0579](#) [hep-ph]].
- [44] J. H. Heo, Phys. Lett. B **693** (2010) 255 [[arXiv:0901.3815](#) [hep-ph]].
- [45] S. Gardner, Phys. Rev. D **79** (2009) 055007 [[arXiv:0811.0967](#) [hep-ph]].
- [46] E. Masso, S. Mohanty and S. Rao, Phys. Rev. D **80** (2009) 036009 [[arXiv:0906.1979](#) [hep-ph]].
- [47] T. Banks, J. -F. Fortin and S. Thomas, [arXiv:1007.5515](#) [hep-ph].
- [48] J. -F. Fortin and T. M. P. Tait, Phys. Rev. D **85** (2012) 063506 [[arXiv:1103.3289](#) [hep-ph]].
- [49] V. Barger, W. -Y. Keung, D. Marfatia and P. -Y. Tseng, [arXiv:1206.0640](#) [hep-ph].
- [50] J. M. Cline, Z. Liu and W. Xue, [arXiv:1201.4858](#) [hep-ph].
- [51] R. Foadi, M. T. Frandsen, T. A. Ryttov and F. Sannino, Phys. Rev. D **76** (2007) 055005 [[arXiv:0706.1696](#) [hep-ph]].
- [52] T. A. Ryttov and F. Sannino, Phys. Rev. D **78** (2008) 115010 [[arXiv:0809.0713](#) [hep-ph]].
- [53] F. Sannino and R. Zwicky, Phys. Rev. D **79**, 015016 (2009) [[arXiv:0810.2686](#) [hep-ph]].
- [54] F. Sannino, Acta Phys. Polon. B **40** (2009) 3533 [[arXiv:0911.0931](#) [hep-ph]].
- [55] E. Nardi, F. Sannino and A. Strumia, JCAP **0901**, 043 (2009) [[arXiv:0811.4153](#) [hep-ph]].
- [56] R. Lewis, C. Pica and F. Sannino, Phys. Rev. D **85**, 014504 (2012) [[arXiv:1109.3513](#) [hep-ph]].
- [57] N. Fornengo, P. Panci and M. Regis, Phys. Rev. D **84** (2011) 115002 [[arXiv:1108.4661](#) [hep-ph]].
- [58] E. J. Chun, J. -C. Park, S. Scopel, JHEP **1102** (2011) 100. [[arXiv:1011.3300](#) [hep-ph]].
- [59] E. Del Nobile and F. Sannino, [arXiv:1102.3116](#) [hep-ph]. Accepted for publication.
- [60] R. Foadi, M. T. Frandsen and F. Sannino, Phys. Rev. D **80** (2009) 037702 [[arXiv:0812.3406](#) [hep-ph]].
- [61] M. T. Frandsen and F. Sannino, Phys. Rev. D **81** (2010) 097704 [[arXiv:0911.1570](#) [hep-ph]].

- [62] Particle Data Group webpage of Atomic and Nuclear Properties.
- [63] N. J. Stone, “Table of Nuclear Magnetic Dipole and Electric Quadrupole Moments” released by the IAEA Nuclear Data Services.
- [64] A. L. Fitzpatrick, W. Haxton, E. Katz, N. Lubbers and Y. Xu, [arXiv:1203.3542](#) [hep-ph].
- [65] R. H. Helm, Phys. Rev. **104**, (1956), 1466.
- [66] N. Fornengo and S. Scopel, Phys. Lett. B **576** (2003) 189 [[hep-ph/0301132](#)].
- [67] E. Del Nobile, C. Kouvaris, F. Sannino and J. Virkajarvi, [arXiv:1111.1902](#) [hep-ph].
- [68] X. Gao, Z. Kang, T. Li, [[arXiv:1107.3529](#) [hep-ph]].
- [69] M. Pato, JCAP **1110** (2011) 035 [[arXiv:1106.0743](#) [astro-ph.CO]].
- [70] S. -L. Chen and Y. Zhang, Phys. Rev. D **84** (2011) 031301 [[arXiv:1106.4044](#) [hep-ph]].
- [71] M. T. Frandsen, F. Kahlhoefer, S. Sarkar and K. Schmidt-Hoberg, JHEP **1109** (2011) 128 [[arXiv:1107.2118](#) [hep-ph]].
- [72] A. Kurylov, M. Kamionkowski, Phys. Rev. **D69** (2004) 063503. [[hep-ph/0307185](#)].
- [73] J. M. Cline and A. R. Frey, Phys. Rev. D **84** (2011) 075003 [[arXiv:1108.1391](#) [hep-ph]].
- [74] J. M. Cline and A. R. Frey, Phys. Lett. B **706** (2012) 384 [[arXiv:1109.4639](#) [hep-ph]].
- [75] R. Bernabei *et al.* [DAMA Collaboration], Nucl. Instrum. Meth. **A592**, (2008), 297, [[arXiv:0804.2738](#) [astro-ph]].
- [76] R. Bernabei, P. Belli, V. Landoni, F. Montecchia, W. Di Nicolantonio, A. Incicchitti, D. Prospero and C. Bacci *et al.*, Phys. Lett. B **389** (1996) 757.
- [77] C. E. Aalseth *et al.* [CoGeNT Collaboration], Phys. Rev. Lett. **101**, (2008), 251301. [[arXiv:0807.0879](#) [astro-ph]].
- [78] P. S. Barbeau, J. I. Collar and O. Tench, JCAP **0709**, (2007), 009, [[arXiv:nucl-ex/0701012](#)].
- [79] Z. Ahmed *et al.* [CDMS-II and CDMS Collaborations], Phys. Rev. D **83** (2011) 112002 [[arXiv:1012.5078](#) [astro-ph.CO]].
- [80] Z. Ahmed *et al.* [CDMS and EDELWEISS Collaborations], Phys. Rev. D **84** (2011) 011102 [[arXiv:1105.3377](#) [astro-ph.CO]].
- [81] E. Aprile *et al.* [XENON100 Collaboration], Phys. Rev. D **84** (2011) 052003 [[arXiv:1103.0303](#) [hep-ex]].
- [82] R. E. Apfel, Nucl. Inst. and Meth. 162 (1979) 603–608.
- [83] H. Ing, R. Noulty, T. McLean, Radiation Measurements 27 (1997) 1–11.

- [84] E. Komatsu *et al.* [WMAP Collaboration], *Astrophys. J. Suppl.* **192** (2011) 18 [[arXiv:1001.4538](#) [astro-ph.CO]].
- [85] P. Gondolo and G. Gelmini, *Nucl. Phys. B* **360** (1991) 145.
- [86] A. Belyaev, M. T. Frandsen, S. Sarkar and F. Sannino, *Phys. Rev. D* **83**, 015007 (2011) [[arXiv:1007.4839](#) [hep-ph]].
- [87] M. Cirelli, P. Panci, G. Servant and G. Zaharijas, *JCAP* **1203**, 015 (2012) [[arXiv:1110.3809](#) [hep-ph]].
- [88] S. Tulin, H. -B. Yu and K. M. Zurek, [arXiv:1202.0283](#) [hep-ph].
- [89] M. R. Buckley and S. Profumo, *Phys. Rev. Lett.* **108**, 011301 (2012) [[arXiv:1109.2164](#) [hep-ph]].
- [90] S. Galli, F. Iocco, G. Bertone and A. Melchiorri, *Phys. Rev. D* **80** (2009) 023505 [[arXiv:0905.0003](#) [astro-ph.CO]].
- [91] T. R. Slatyer, N. Padmanabhan and D. P. Finkbeiner, *Phys. Rev. D* **80** (2009) 043526 [[arXiv:0906.1197](#) [astro-ph.CO]].
- [92] G. Huetsi, A. Hektor and M. Raidal, *Astron. Astrophys.* **505** (2009) 999 [[arXiv:0906.4550](#) [astro-ph.CO]].
- [93] M. Cirelli, F. Iocco and P. Panci, *JCAP* **0910** (2009) 009 [[arXiv:0907.0719](#) [astro-ph.CO]].
- [94] G. Huetsi, J. Chluba, A. Hektor and M. Raidal, *Astron. Astrophys.* **535** (2011) A26 [[arXiv:1103.2766](#) [astro-ph.CO]].
- [95] S. Galli, F. Iocco, G. Bertone and A. Melchiorri, *Phys. Rev. D* **84** (2011) 027302 [[arXiv:1106.1528](#) [astro-ph.CO]].
- [96] M. Ackermann *et al.* [Fermi-LAT Collaboration], *Phys. Rev. Lett.* **107** (2011) 241302 [[arXiv:1108.3546](#) [astro-ph.HE]].
- [97] M. Cirelli, P. Panci and P. D. Serpico, *Nucl. Phys. B* **840** (2010) 284 [[arXiv:0912.0663](#) [astro-ph.CO]].
- [98] M. Papucci and A. Strumia, *JCAP* **1003** (2010) 014 [[arXiv:0912.0742](#) [hep-ph]].
- [99] G. Zaharijas *et al.* [for the Fermi-LAT Collaboration], *PoS IDM* **2010** (2011) 111 [[arXiv:1012.0588](#) [astro-ph.HE]].
- [100] A. A. Abdo *et al.*, *Phys. Rev. Lett.* **104** (2010) 091302 [[arXiv:1001.4836](#) [astro-ph.HE]].
- [101] Talk given by A. Morselli at the [7th International workshop on Dark Side of the Universe](#).
- [102] J. Goodman, M. Ibe, A. Rajaraman, W. Shepherd, T. M. P. Tait and H. -B. Yu, *Nucl. Phys. B* **844** (2011) 55 [[arXiv:1009.0008](#) [hep-ph]].

- [103] C. Kouvaris and P. Tinyakov, Phys. Rev. Lett. **107**, 091301 (2011) [[arXiv:1104.0382](#) [astro-ph.CO]].
- [104] S. D. McDermott, H. -B. Yu and K. M. Zurek, Phys. Rev. D **85**, 023519 (2012) [[arXiv:1103.5472](#) [hep-ph]].
- [105] T. Guver, A. E. Erkoca, M. H. Reno and I. Sarcevic, [arXiv:1201.2400](#) [hep-ph].
- [106] C. Kouvaris, [arXiv:1111.4364](#) [astro-ph.CO].
- [107] C. Kouvaris and P. Tinyakov, Phys. Rev. D **83**, 083512 (2011) [[arXiv:1012.2039](#) [astro-ph.HE]].